Since January 2020 Elsevier has created a COVID-19 resource centre with free information in English and Mandarin on the novel coronavirus COVID-19. The COVID-19 resource centre is hosted on Elsevier Connect, the company's public news and information website.

Article

Cell

Unexpected Receptor Functional Mimicry Elucidates Activation of Coronavirus Fusion

Graphical Abstract

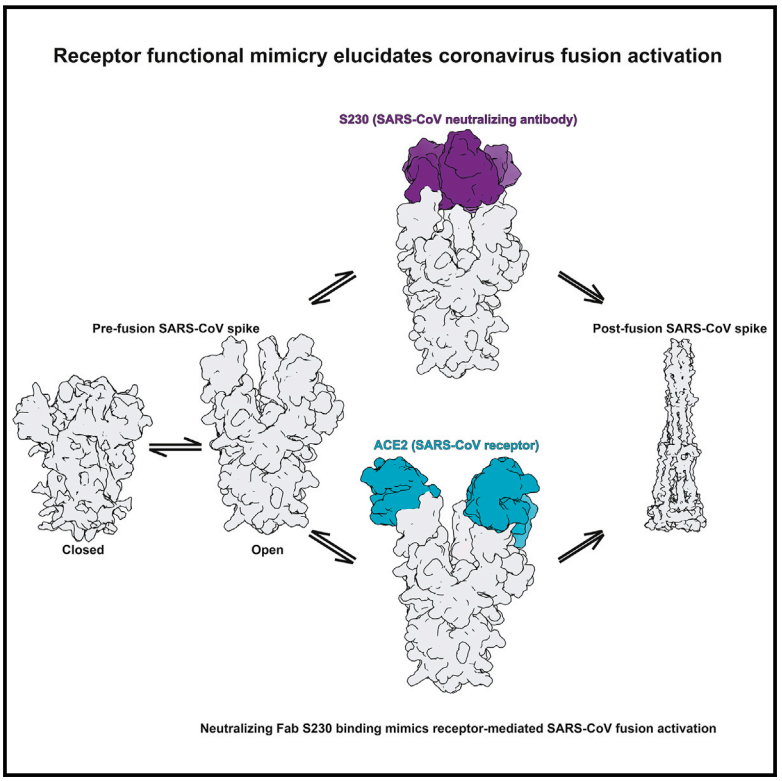

Highlights

- MERS-CoV/SARS-CoV S composite glycan shields analyzed by cryo-EM and mass spectrometry
- Structures of MERS-CoV/SARS-CoV S with neutralizing antibodies from survivors
- LCA60 inhibits receptor binding by interacting with MERS-CoV S protein/glycans
- S230 blocks receptor binding and triggers fusogenic rearrangements via functional mimicry

Authors

Alexandra C. Walls, Xiaoli Xiong, Young-Jun Park, ..., Félix A. Rey, Davide Corti, David Veesler

Correspondence

dveesler@uw.edu

In Brief

Structural analysis of the SARS-CoV S and MERS-CoV S glycoproteins in complex with neutralizing antibodies from human survivors sheds light into the mechanisms of membrane fusion and neutralization

Walls et al., 2019, Cell *176*, 1026–1039
February 21, 2019
https://doi.org/10.1016/j.cell.2018.12.028

CellPress

Cell

Article

Unexpected Receptor Functional Mimicry Elucidates Activation of Coronavirus Fusion

Alexandra C. Walls,[1,7] Xiaoli Xiong,[1,7] Young-Jun Park,[1] M. Alejandra Tortorici,[1,2] Joost Snijder,[1] Joel Quispe,[1] Elisabetta Cameroni,[3] Robin Gopal,[4] Mian Dai,[5] Antonio Lanzavecchia,[6] Maria Zambon,[4] Félix A. Rey,[2] Davide Corti,[3] and David Veesler[1,8,*]

[1]Department of Biochemistry, University of Washington, Seattle, Washington 98195, USA
[2]Institute Pasteur & CNRS UMR 3569, Unité de Virologie Structurale, 75015, Paris, France
[3]Humabs Biomed SA, Vir Biotechnology, 6500 Bellinzona, Switzerland
[4]National Infection Service, Public Health England, London NW9 5HT, UK
[5]Crick Worldwide Influenza Centre, The Francis Crick Institute, 1 Midland Road, London NW1 1AT, UK
[6]Institute for Research in Biomedicine, Faculty of Biomedical Sciences, Università della Svizzera italiana, 6500 Bellinzona, Switzerland
[7]These authors contributed equally
[8]Lead Contact
*Correspondence: dveesler@uw.edu
https://doi.org/10.1016/j.cell.2018.12.028

SUMMARY

Recent outbreaks of severe acute respiratory syndrome and Middle East respiratory syndrome, along with the threat of a future coronavirus-mediated pandemic, underscore the importance of finding ways to combat these viruses. The trimeric spike transmembrane glycoprotein S mediates entry into host cells and is the major target of neutralizing antibodies. To understand the humoral immune response elicited upon natural infections with coronaviruses, we structurally characterized the SARS-CoV and MERS-CoV S glycoproteins in complex with neutralizing antibodies isolated from human survivors. Although the two antibodies studied blocked attachment to the host cell receptor, only the anti-SARS-CoV S antibody triggered fusogenic conformational changes via receptor functional mimicry. These results provide a structural framework for understanding coronavirus neutralization by human antibodies and shed light on activation of coronavirus membrane fusion, which takes place through a receptor-driven ratcheting mechanism.

INTRODUCTION

Coronaviruses are enveloped viruses responsible for up to 30% of mild respiratory tract infections and atypical pneumonia in humans. The severe acute respiratory syndrome coronavirus (SARS-CoV) emerged in 2002 in the Guangdong province of China and spread across the globe, resulting in 8,000 infections and nearly 800 deaths in 37 countries. The Middle East respiratory syndrome coronavirus (MERS-CoV) emerged in the Arabian peninsula in 2012 and has caused numerous outbreaks in humans, with a fatality rate of 35%. SARS-CoV is of bat origin and crossed the species barrier using palm civets as putative intermediate hosts (Ge et al., 2013; Li et al., 2005b; Wang et al., 2005), whereas MERS-CoV is found in dromedary camels as a natural reservoir (Haagmans et al., 2014; Memish et al., 2013). Surveillance studies in bats detected numerous coronaviruses sharing high nucleotide sequence similarity with pathogenic human coronaviruses (Hu et al., 2017; Menachery et al., 2015, 2016), suggesting that additional zoonotic transmission events are likely to occur in the future. Currently, no specific treatments or vaccines are available against any of the six human-infecting coronaviruses.

Coronavirus entry into host cells is mediated by the trimeric transmembrane spike (S) glycoprotein. S is composed of two functional subunits responsible for binding to the host cell receptor (S_1 subunit) and fusion of the viral and cellular membranes (S_2 subunit) (Gui et al., 2017; Kirchdoerfer et al., 2016; Pallesen et al., 2017; Shang et al., 2017, 2018; Walls et al., 2016a, 2016b, 2017; Xiong et al., 2017; Yuan et al., 2017). We have previously determined structures of the mouse hepatitis virus (MHV) S ectodomain in the pre-fusion and post-fusion states, which provided snapshots of the start and end points of the membrane fusion reaction (Walls et al., 2016a, 2017). These studies demonstrated that membrane fusion involves large conformational changes in the C-terminal (S_2) subunit, similarly to other class I fusion proteins.

Proteolytic processing and receptor-binding act in synergy to induce large-scale S conformational changes promoting coronavirus entry. Priming involves S cleavage by host proteases at the boundary between the S_1 and S_2 subunits (S_1/S_2), in a subset of coronaviruses, and at a conserved site upstream of the fusion peptide (S_2') in all known coronaviruses (Belouzard et al., 2009; Burkard et al., 2014; Millet and Whittaker, 2014; Park et al., 2016). The latter site is believed to be the most important for membrane fusion activation. The SARS-CoV and MERS-CoV S receptor-binding domain, designated domain B, exhibits multiple conformational states that modulate the accessibility of the receptor-binding motifs (RBMs) and in turn the ability to interact with host cells. Based on these findings, it was hypothesized that receptor binding may initiate membrane fusion (Gui et al., 2017; Pallesen et al., 2017; Yuan et al., 2017). However, the S glycoprotein of other coronaviruses adopt a closed domain B

conformation, incompatible with receptor engagement, indicating that structural rearrangements prior to receptor binding are required for entry (Kirchdoerfer et al., 2016; Shang et al., 2017, 2018; Walls et al., 2016a, 2016b; Xiong et al., 2017). Due to this unusual mechanism of proteolytic activation and RBM conformational masking, our understanding of coronavirus membrane fusion activation remains limited.

Since the S glycoprotein densely decorates the viral surface and is a key player in pathogenesis, it is the main target of neutralizing antibodies and the focus of intense interest for vaccine design. We previously showed that coronavirus S glycoproteins are decorated with an extensive glycan shield comprising up to 100 N-linked oligosaccharides (Walls et al., 2016b; Xiong et al., 2017). Molecular-level information of the carbohydrates attached to the surface of highly pathogenic coronaviruses, however, is lacking. These glycans contribute to S stability during biogenesis, since inhibition of glycosylation by tunicamycin was reported to yield virions lacking S glycoproteins (Rossen et al., 1998) and likely participate in immune evasion via epitope masking (Du et al., 2016; Walls et al., 2016b; Xiong et al., 2017). Studies of the S glycoproteins of MERS-CoV and the bat-specific HKU4 coronavirus suggested that glycans also impact zoonosis by modulating cleavage-site accessibility to proteases for membrane-fusion activation (Yang et al., 2015). The outcome of the arms race between viral evolution mechanisms and the immune system of infected individuals can also lead to the elicitation of antibodies binding glycan-containing epitopes, such as in the case of HIV-1 (Scharf et al., 2015; Stewart-Jones et al., 2016) or Epstein-Barr virus (Snijder et al., 2018). These findings emphasize the necessity to obtain a detailed understanding of the carbohydrates covering coronavirus S glycoproteins to accelerate the development of subunit vaccines and therapeutics.

We previously reported the isolation of highly potent monoclonal neutralizing antibodies from rare memory B cells obtained from SARS-CoV and MERS-CoV survivors (Corti et al., 2015; Traggiai et al., 2004). To understand neutralization, we report here an analysis of the fine molecular structure of the SARS-CoV and MERS-CoV S glycan shields and the cryoelectron microscopy (cryo-EM) study of these glycoproteins in complex with two potent human neutralizing antibodies. Although both antibodies block receptor interaction, the anti-SARS-CoV antibody acts by functionally mimicking receptor attachment and promoting S fusogenic conformational rearrangements through a ratcheting mechanism. We found that the dynamics of the receptor-binding domain alter the apparent binding affinity of coronavirus S trimers for their cognate receptors, a phenomenon that cannot be detected using isolated B domains. The findings presented here elucidate the unique nature of the coronavirus membrane-fusion activation pathway.

RESULTS

The MERS-CoV and SARS-CoV S Glycan Shields

We set out to obtain a blueprint of individual N-linked carbohydrates attached to the surface of the MERS-CoV and SARS-CoV S glycoproteins produced in HEK293F cells. We used the stabilized MERS-CoV S 2P and SARS-CoV S 2P ectodomains, which harbor a double proline substitution between the central helix and the heptad-repeat 1 motif to enhance the stability of the prefusion conformation (Pallesen et al., 2017). We determined that oligosaccharides account for a molecular weight of 121 kDa and 98 kDa for MERS-CoV and SARS-CoV S, respectively (Figures S1A and S1B), using multi-angle light scattering, refractometry, and UV spectrophotometry (Veesler et al., 2009). These results suggest that ~25% of the molecular weight of a S ectodomain corresponds to oligosaccharides, whereas 50% of the HIV-1 mosaic M Env molecular weight is accounted for by glycans (Nkolola et al., 2014). We detected N-linked glycosylations at 22 and 16 unique sites for the MERS-CoV and SARS-CoV S protomers, respectively, using liquid chromatography coupled with electron transfer/high-energy collision dissociation tandem mass spectrometry (LC-MS/MS) (Frese et al., 2013). The data revealed an extraordinary heterogeneity of carbohydrates decorating the two S trimers (Figures 1A and 1B and Tables S1 and S2). Individual sequons were linked to 21 unique glycans on average and up to 64 distinct oligosaccharides for the most heterogeneous sites. The intact glycopeptides were a variety of oligomannose, hybrid, and complex glycans, with or without sialylation and (core) fucosylation. Most of the observed diversity corresponded to hybrid/complex carbohydrates (Figures 1A, 1B, S1C, and S1D and Tables S1 and S2). The detection of glycans with different extent of processing on coronavirus S glycoproteins is reminiscent of the composite nature of the HIV Env (Struwe et al., 2018) or Lassa virus GP (Watanabe et al., 2018) glycan shields. The large number and combinatorial diversity of N-linked glycans covering the surface of MERS-CoV and SARS-CoV S could represent a challenge to overcome for antigen recognition.

Previous observations of SARS-CoV budding directly from the endoplasmic reticulum-Golgi intermediate compartment (ERGIC) and/or from swollen Golgi sacs led to the hypothesis that coronaviruses might only be exposed to a subset of the enzymes of the glycosylation machinery (Ng et al., 2003; Stertz et al., 2007). To address this question, we used LC-MS/MS to characterize in parallel S oligosaccharides on the MERS-CoV England1 and Erasmus Medical Center (EMC)/2012 isolates produced using African green monkey VeroE6 cells, as well as on the purified MERS-CoV S 2P ectodomain trimer recombinantly produced using HEK293F cells. We observed extensive overlap of the types of glycans detected across virion-derived and ectodomain-derived MERS-CoV samples, including the presence of hybrid and complex glycans (Figures S2A and S2B and Tables S1, S2, and S3). Our data agree with previous work detecting hybrid/complex glycans N-linked to S present in the membrane of authentic SARS-CoV virions (Krokhin et al., 2003; Ritchie et al., 2010), which is consistent with our analysis of the SARS-CoV S 2P ectodomain trimer. Our data indicate that at least a fraction of the MERS-CoV and SARS-CoV virions produced in a cell are exposed to the glycan-processing enzymes residing in the Golgi apparatus during assembly and budding.

The asymmetric cryoEM reconstructions of MERS-CoV S and SARS-CoV S in complex with human antibodies presented in the following sections respectively resolve glycan densities at 17 and 19 sites, virtually all of them overlapping with the MS/MS data (Figures 1C and 1D). At least the two core N-acetyl glucosamine moieties are resolved for the

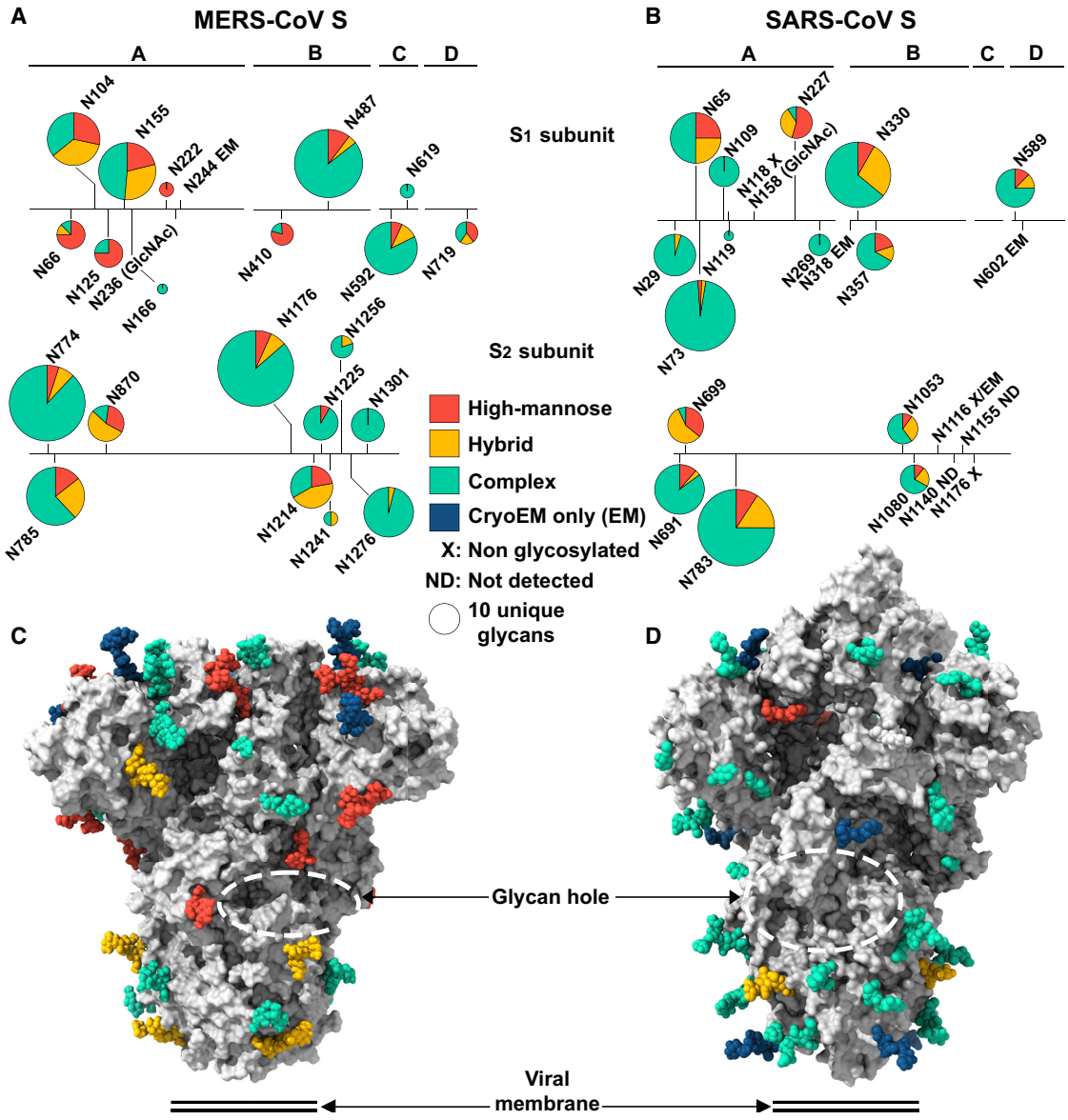

Figure 1. Characterization of the S Glycan Shield of MERS-CoV and SARS-CoV S Glycoproteins

(A and B) Analysis of the glycans N-linked to MERS-CoV S 2P (A) and SARS-CoV S 2P (B) ectodomain trimers expressed using HEK293F cells. Each site is represented by a pie chart colored according to the processing state detected by LC-MS/MS and for which the diameter is scaled based on the number of unique glycopeptides identified. Glycan assignment was performed as follows: high-mannose, 2 HexNAc; hybrid, 3 HexNAc; complex, ≥4 HexNAc; GlcNAc, N-acetyl glucosamine (detected for endo-H-treated samples).

(C and D) Surface representation of the fully glycosylated MERS-CoV S 2P (C) and SARS-CoV S 2P (D) ectodomain trimers (gray) with N-linked glycans rendered as spheres colored according to the processing state (i.e., corresponding to the largest number of unique N-linked glycans identified by LC-MS/MS, as in A and B).

Domains A–D are labeled in (A) and (B). (C) and (D) were generated using the MERS-CoV S2P/LCA60 and SARS-CoV S2P/S230 structures for which the Fabs were removed for clarity. See also Figures S1 and S2 and Tables S1, S2, and S3.

majority of glycosylation sites, which extend from the surface of both the S_1 and S_2 subunits. Although both glycoproteins are densely decorated with N-linked glycans, by comparison, the surface of the HIV Env trimer is obstructed by twice as many glycans per accessible surface area. MERS-CoV S and SARS-CoV S trimers share that the regions surrounding the S_1/S_2 cleavage site and the fusion peptide (near the S_2 cleavage site) are more sparsely glycosylated than the rest of each trimer (Figures 1C and 1D). These glycan holes could be important for providing access to activating host proteases and for allowing membrane fusion to take place unimpeded at the onset of infection (Walls et al., 2017; Yang et al., 2015). We

suggest that the identified glycan holes could be exploited for epitope-focused immunogen design or therapeutic intervention against coronaviruses. This is supported by the presence of neutralizing antibodies targeting the fusion peptide region in SARS-CoV survivor sera (Zhang et al., 2004), the high sequence conservation of this region among coronavirus S glycoproteins (Walls et al., 2016a), and the identification of a neutralization epitope within a comparable breach of the HIV-1 Env glycan shield (McCoy et al., 2016).

Structure of the MERS-CoV S Glycoprotein in Complex with the Human LCA60 Antibody

The LCA60 antibody was isolated from memory B cells of a MERS-CoV-infected individual and potently neutralized multiple MERS-CoV isolates (i.e., England1, EMC/2012, and Jordan-N3/2012) (Corti et al., 2015). Cryo-EM analysis of the stabilized MERS-CoV S 2P glycoprotein ectodomain in complex with the LCA60 Fab fragment showed full saturation with one Fab bound to each B domain of the homotrimeric S. 3D classification revealed that the complex adopts two distinct conformational states (Figures 2A–2D and S3A–S3E and Table S4), corresponding to two B domains closed and one B domain open (state 1, ~50%), as well as one B domain closed and two B domains open (state 2, ~50%). We determined asymmetric cryoEM reconstructions at 3.5 Å and 3.6 Å resolution for states 1 and 2, respectively (Figures 2A–2D and S3C–S3E and Table S4), as well as a crystal structure of the isolated LCA60 Fab at 3.0 Å resolution (Table S5). LCA60 Fabs bound to open B domains are weakly resolved in the maps, suggesting marked conformational heterogeneity, whereas the quality of the density is enhanced for closed LCA60/B domains despite radial disorder (Figures S3D and S3E). Analysis of the S/LCA60 contacts was done using the state 1 structure.

LCA60 CDRH2, CDRH3, CDRL1, and CDRL3 interact with the MERS-CoV B domain (Figures 3A and 3B), which also mediates binding to human dipeptidyl-peptidase 4 (DPP4), the MERS-CoV receptor (Raj et al., 2013). The binding interface of LCA60 and MERS-CoV S involves protein/protein and protein/glycan contacts. The 17-residue long CDRH3 contacts the β8 strand and the preceding loop within the RBM. Specifically, residue $W108_{LCA60}$ inserts between the B domain residues $P531_{MERS\text{-}CoV}$ and $Y541_{MERS\text{-}CoV}$ on one side and the glycan N-linked to the A domain residue $N166_{MERS\text{-}CoV}$ from a neighboring protomer on the other side (Figures 3C and S4). CDRH2 also contacts the loop preceding strand β8 via electrostatic interactions. CDRL3 contacts the MERS-CoV strands β6 and β9 and the loop preceding strand β8, whereas CDRL1 interacts with the loops preceding strands β6 and β8 (Figures 3A–3C). Domain A glycans at positions $N166_{MERS\text{-}CoV}$ and $N236_{MERS\text{-}CoV}$ appear to contact the Fab bound to the B domain of a neighboring protomer (Figures 3A–3D and S4). The glycan N-linked to $N487_{MERS\text{-}CoV}$ of one protomer extends toward the Fab CDRH2 bound to the closed B domain of the neighboring protomer (Figure 3D) but is much less well resolved or unresolved in the other two protomers due to the absence of contact with neighboring LCA60 Fabs. The multiple contacts observed between LCA60 and oligosaccharides on the surface of the protein illustrates that the antibody accommodates MERS-CoV S glycan for binding and neutralization. Since the residues participating to the epitope and the glycosylation sequons at positions N166, N236, and N487 are conserved in >99.5% of MERS-CoV isolates, LCA60 is predicted to broadly neutralize most MERS-CoV viruses sequenced to date, although the chemical composition and occupancy of each glycan could modulate binding. LCA60 therefore shares similarities with several HIV-1 broadly neutralizing antibodies, which interact to varying degree with carbohydrates N-linked to the Env glycoprotein (Scharf et al., 2015; Stewart-Jones et al., 2016).

Our structure rationalizes the effect of the previously described $E536A_{MERS\text{-}CoV}$ escape mutant that would disrupt putative electrostatic interactions with CDRH2 residues $R50_{LCA60}$ and $K52_{LCA60}$ and/or CDRH3 residue $R103_{LCA60}$ (Corti et al., 2015) (Figure 3C). It also suggests that the $K493E_{MERS\text{-}CoV}$ substitution could alter the positioning of the β5-β6 loop, which might in turn prevent CDRL1 from approaching the B domain, thereby providing a potential explanation for the observed loss of binding (Corti et al., 2015). The $T489A_{MERS\text{-}CoV}$ substitution would remove the glycan that extends toward the Fab CDRH2 bound to the closed B domain of the neighboring protomer (Figure 3D). The observed abrogation of LCA60 binding for the $T489A_{MERS\text{-}CoV}$ mutant (Corti et al., 2015) might be explained by a loss of these protein/glycan contacts, although only one out of the three bound Fabs interact with the glycan at position $N487_{MERS\text{-}CoV}$.

Comparison of the MERS-CoV S/LCA60 structure with the crystal structure of the MERS-CoV B domain in complex with DPP4 (Lu et al., 2013) shows that the two proteins would clash upon binding to MERS-CoV S and that the Fab and receptor epitopes partially overlap (Figures 3E and 3F). This observation supports the finding that LCA60 and DPP4 compete for binding to MERS-CoV S (Corti et al., 2015). Whereas LCA60 can bind to all possible conformations of the B domain, DPP4 binding strictly requires opening of the B domain due to burial of its binding site in the closed conformation.

Structure of the SARS-CoV S Glycoprotein in Complex with the Human S230 Antibody

The S230 antibody was isolated from memory B cells of a SARS-CoV-infected individual and potently neutralized a broad spectrum of SARS-CoV isolates of human and animal origin (Rockx et al., 2008; Traggiai et al., 2004). Cryo-EM characterization of the stabilized SARS-CoV S 2P glycoprotein in complex with the S230 Fab revealed that the particle images could be divided into SARS-CoV S/S230 complex with (state 1) or without (state 2) one closed B domain (Figures 4A–4D and S3F–S3J and Table S4). 3D classification of the cryo-EM data revealed that the state 1 complex features multiple orientations of each of the two S230 Fabs associated with intermediate and open conformations of the B domains. In the SARS-CoV S/S230 state 2 complex structure, the three B domains are open, albeit with conformations deviating from 3-fold symmetry, with the three bound Fabs protruding away from the S trimer apex (Figures 4C and 4D). We obtained asymmetric reconstructions at 4.2 Å and 4.5 Å resolution of the SARS-CoV S/S230 complex in states 1 and 2, respectively (Figures 4A–4D and S3H–S3J and Table S4). The large conformational heterogeneity of the SARS-CoV S/S230

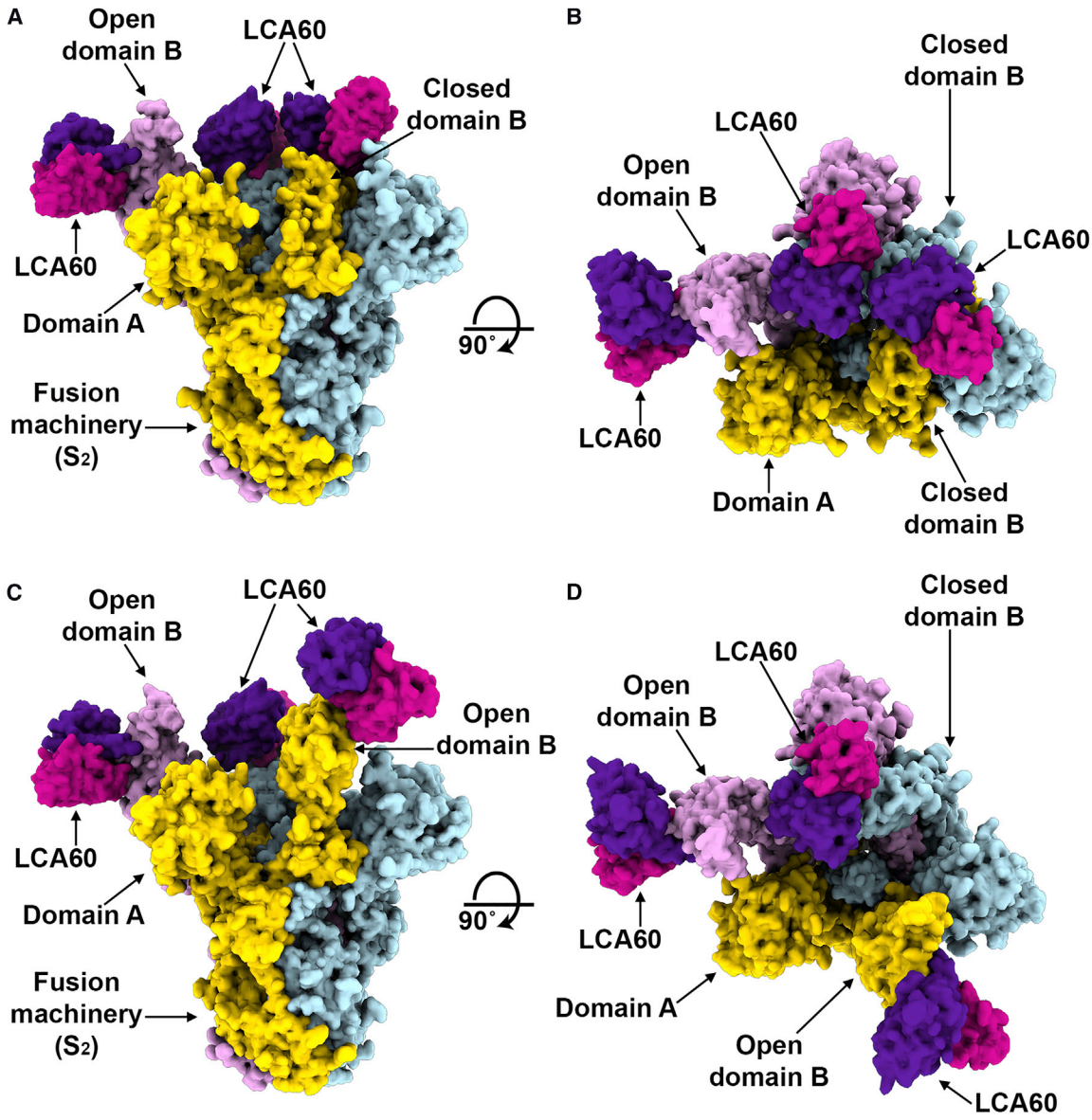

Figure 2. CryoEM Structures of the MERS-CoV S Glycoprotein in Complex with the LCA60 Neutralizing Antibody

(A and B) Orthogonal views of the state 1 structure with one open and two closed B domains.

(C and D) Orthogonal views of the state 2 structure with two open and one closed B domains.

The structures are rendered as molecular surfaces with different colors for each S protomer (light blue, plum, and gold) and the LCA60 Fab heavy (purple) and light (pink) chains (only the variable domains are shown). The open B domains/Fabs are only included for visualization and were omitted from the final models. See also Figures S3 and S4 and Tables S4 and S5.

complex contrasts with the limited number of structural states detected for the MERS-CoV S/LCA60 complex. The marked mobility of the B domain/S230 regions, which adopt a continuum of conformations in both structures, limited the resolution of this part of the map. We therefore determined a crystal structure of the isolated S230 Fab at 1.5 Å resolution to assist interpretation of the data (Table S5).

Docking the S230 crystal structure in the cryo-EM map indicated that CDRH2, CDRH3, CDRL1, and CDRL3 contact the B domain (Figures 5A and 5B), which also mediates binding to human angiotensin-converting enzyme 2 (ACE2), the SARS-CoV receptor (Li et al., 2003). The S230 epitope is centered around $L443_{SARS\text{-}CoV}$ and places the CDRH2 residue $F59_{S230}$ and the CDRH3 residues $Y106_{S230}$, $F107_{S230}$, and $Y110_{S230}$ near $Y408_{SARS\text{-}CoV}$, $Y442_{SARS\text{-}CoV}$, $F460_{SARS\text{-}CoV}$, and $Y475_{SARS\text{-}CoV}$. The fitting is therefore consistent with the identification of the $L443R_{SARS\text{-}CoV}$ substitution as the only escape mutant isolated thus far using the SARS-CoV Urbani strain (Rockx et al., 2008), since introduction of a charged residue would affect binding to this epitope.

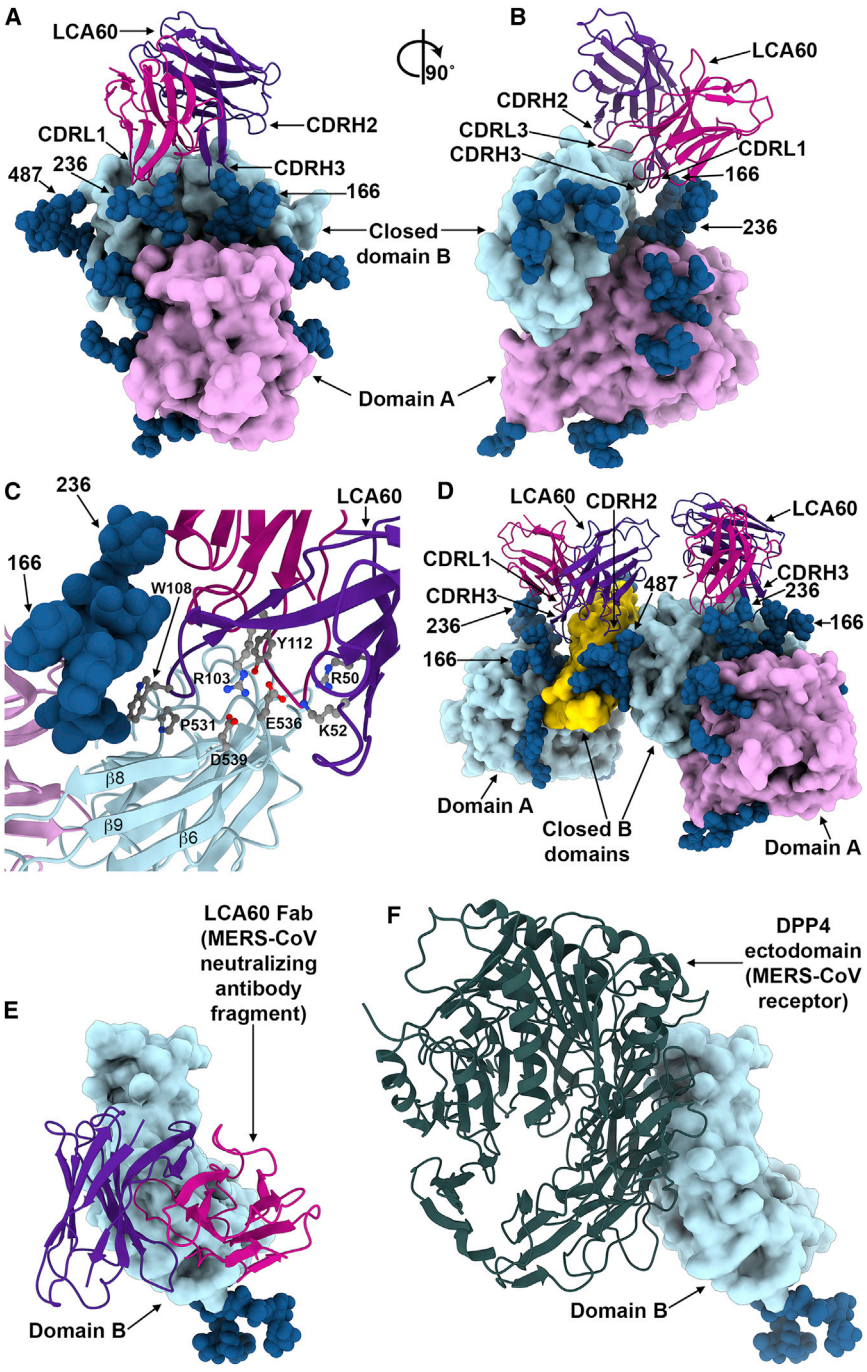

Figure 3. LCA60 Interactions with the MERS-CoV S Receptor-Binding Domain

(A and B) Quasi-orthogonal views of the LCA60 Fab binding to a closed B domain. The A domain from a neighboring protomer is also shown.

(C) Zoomed-in view of the LCA60 CDRH3-mediated contacts. Residues involved in key interactions are shown in ball-and-stick representation colored by atom type (blue: nitrogen, red: oxygen, gray: carbon).

(D) LCA60 Fabs bound to closed B domains in the state 1 structure. The glycan N-linked to N487 of one closed B domain interact with the LCA60 Fab bound to the neighboring closed B domain.

(E and F) LCA60 (E) and DPP4 (F) would clash upon binding to MERS-CoV S and share partially overlapping epitopes on the B domain.

In (A), (B), (D), and (F), S is rendered as molecular surfaces, the Fabs as ribbon diagrams (only the variable domains are shown), and the glycans as blue spheres. In (C), S is rendered as a ribbon diagram. The color scheme is identical to Figure 2. Selected glycans are labeled based on the N-linked glycosylation sequon numbering. See also Figures S3 and S4 and Tables S4 and S5.

Comparison of the SARS-CoV S/S230 structure with the crystal structure of the SARS-CoV B domain in complex with ACE2 (Li et al., 2005a) shows that the two proteins would clash upon binding to SARS-CoV S and that the Fab and receptor epitopes partially overlap (Figures 5C and 5D). This observation supports our previous results, suggesting that S230 and ACE2 compete to bind to SARS-CoV S (Rockx et al., 2008). In contrast to LCA60, which could recognize all possible arrangements of the B domain, S230 only interacts with intermediate and open states, but not with the closed conformation. Since the interaction sites of both S230 and ACE2 are only accessible in the partially or fully open B domain conformations, binding of either of these two proteins to SARS-CoV S would sterically prevent sampling of the closed state (Figures 4A–4D).

Activation Mechanism of Coronavirus Membrane Fusion

Based on the findings that (1) LCA60 and DPP4 or S230 and ACE2 compete to bind to the MERS-CoV or SARS-CoV domain B, respectively (Figures 3E–3F and 5C–5D), and (2) binding of DPP4, S230, or ACE2, but not LCA60, prevents closure of the B domain, we speculated that the conformational changes we captured by cryoEM are related to membrane-fusion triggering. Incubation of the wild-type SARS-CoV S ectodomain trimer (i.e., without stabilizing mutations) with 1.6 μg/mL trypsin (w/v) to recapitulate proteolytic priming led to cleavage at the S_1/S_2 boundary (Belouzard et al., 2009), as observed by SDS-PAGE (Figure S5A). Analysis of the negatively stained sample showed that the SARS-CoV S trimers largely remained in the prefusion conformation and were stable for several days on ice or at room temperature (Figures 6A and 6B). Complex formation between Fab S230 and wild-type SARS-CoV S led to formation of postfusion rosettes, and the frequency of this transition was enhanced with longer incubation times and/or by trypsin cleavage (Figures

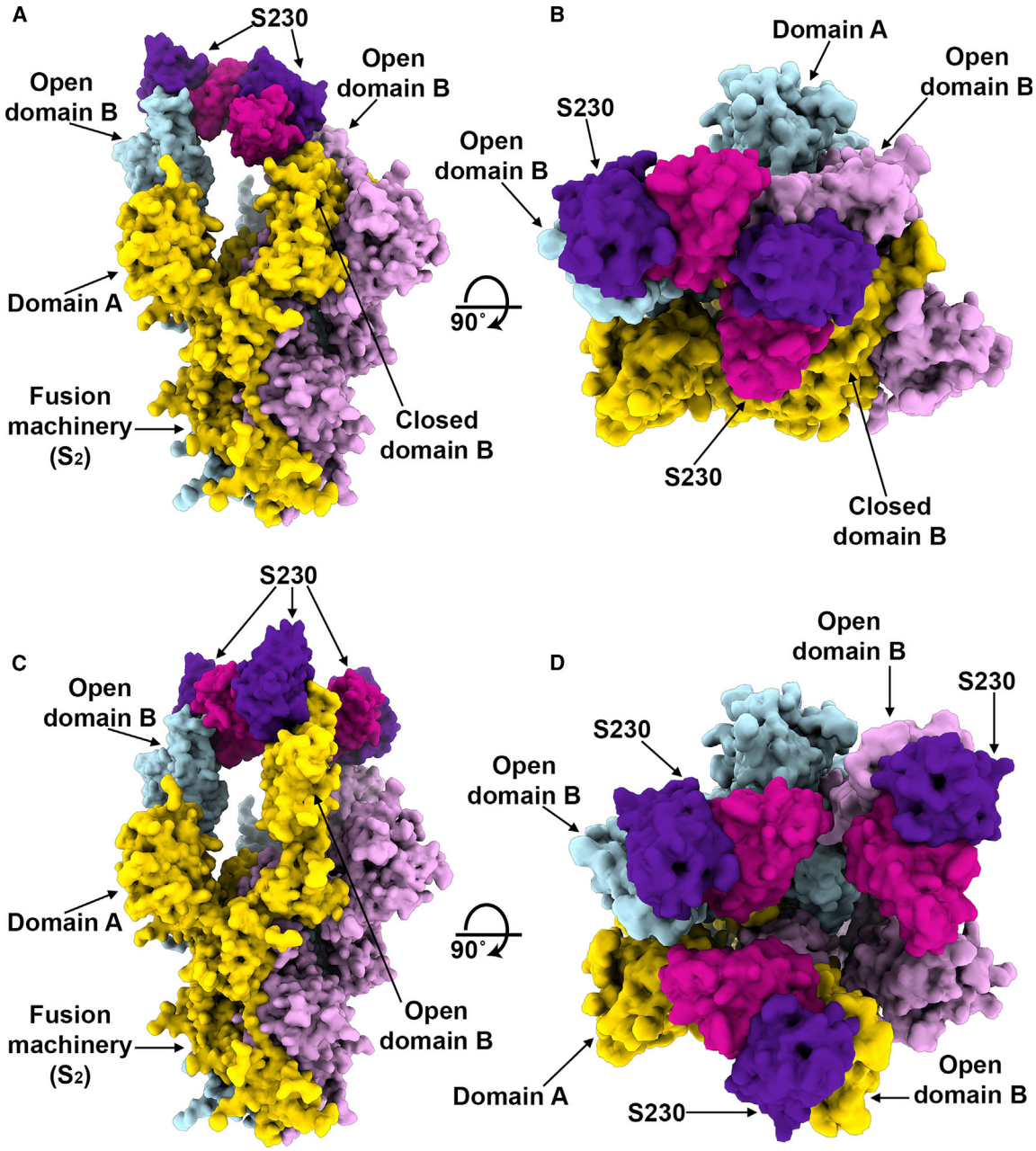

Figure 4. CryoEM Structure of the SARS-CoV S Glycoprotein in Complex with the S230 Neutralizing Antibody

(A and B) Orthogonal views of the state 1 structure with one open, one partially open, and one closed B domain.

(C and D) Orthogonal views of the state 2 structure with three open B domains that do not follow 3-fold symmetry.

The structures are rendered as molecular surfaces with different colors for each S protomer (light blue, plum, and gold) and the LCA60 Fab heavy (purple) and light (pink) chains (only the variable domains are shown). See also Figure S3 and Tables S4 and S5.

6C–6F, S5B, and S5C). The S_1 subunit acts as a "chaperone," contributing to stabilize S_2 in the prefusion state by reducing its propensity to transition to the postfusion conformation. Proteolytic cleavage at the S_1/S_2, S_2' sites or shedding of the S_1 subunit, however, were not strictly required for refolding of the S ectodomain trimer to occur (Figures 6C 6E, 6G, and 6I).

Incubation of the wild-type SARS-CoV S with the ACE2 ectodomain at up to 8 μM (4-fold molar excess) unexpectedly revealed that only a small percentage of the particle images corresponded to complexes, and a limited number of postfusion S trimers could be detected even in the presence of trypsin (Figures 6G–6H and S5D). Prolonged incubation, along with trypsin cleavage, acted in synergy to increase the frequency of refolding, as attested by the presence of postfusion rosettes, although a significant fraction of unbound prefusion S trimers remained (Figures 6I–6J, and S5E, and S5F). We also carried out the

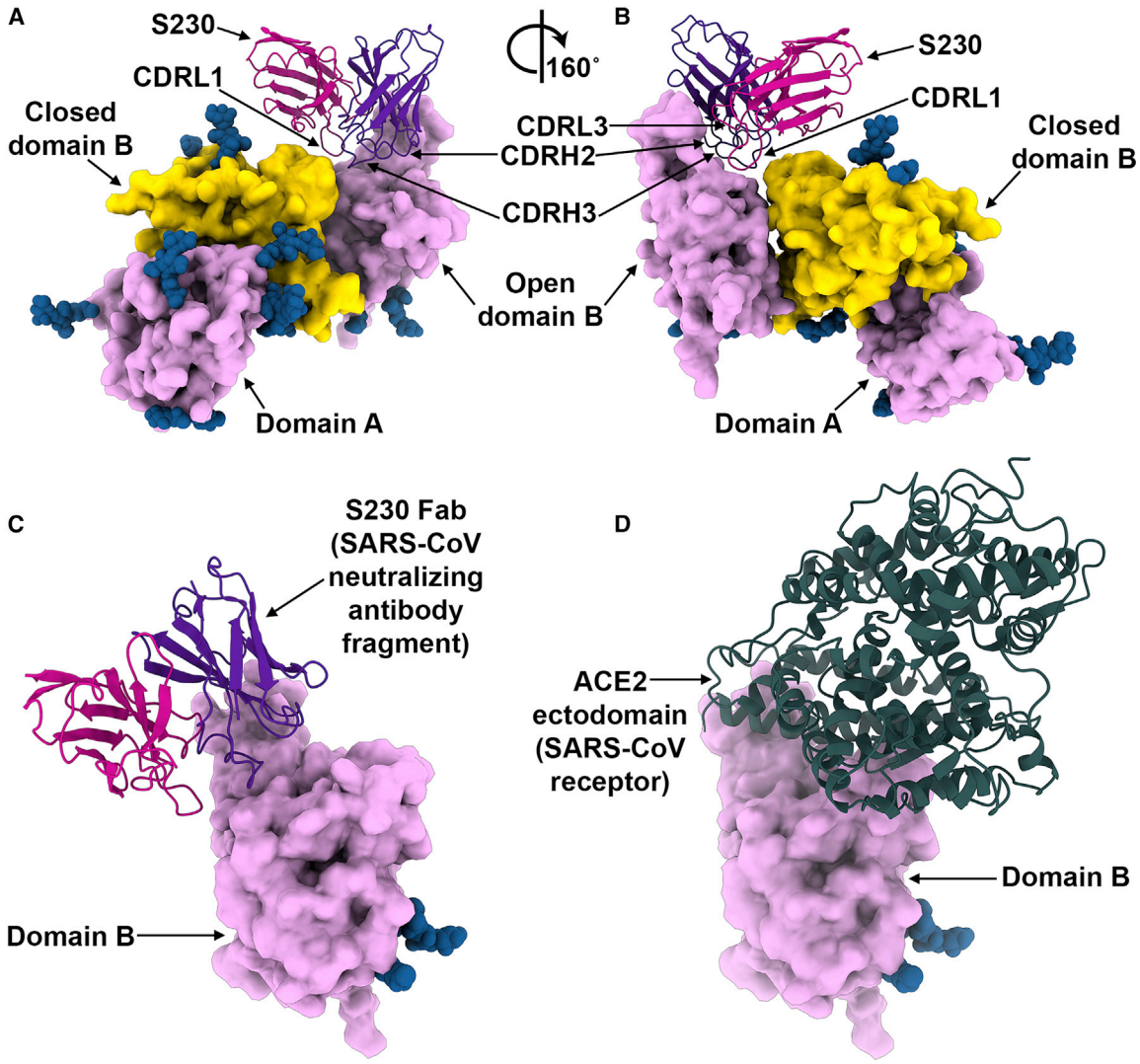

Figure 5. S230 Interactions with the SARS-CoV S Receptor-Binding Domain

(A and B) Two views of the S230 Fab binding to an open B domain. The A domain of the same protomer and B domain from a neighboring protomer are also shown.

(C and D) S230 (C) and ACE2 (D) would clash upon binding to SARS-CoV S and share partially overlapping epitopes on the B domain.

In (A)–(D), S is rendered as molecular surfaces, the Fab as ribbon diagrams (only the variable domains are shown), and the glycans as blue spheres. The color scheme is identical to Figure 4. Selected glycans are labeled based on the N-linked glycosylation sequon numbering. See also Figure S3 and Tables S4 and S5.

same set of experiments with SARS-CoV S pre-incubated with trypsin and similarly observed that S230 was more effective than ACE2 at inducing fusogenic conformational changes (Figures S6A–S6D).

To explore whether these findings could be detected in the context of virions, we analyzed the structural rearrangements of the full-length SARS-CoV S trimer embedded in the membrane of infectious murine leukemia (pseudo)virus (MLV)(Millet and Whittaker, 2016). Refolding of coronavirus S glycoproteins to the postfusion conformation can be detected by the appearance of a proteinase-K-resistant band migrating at approximately 55 kDa when analyzed by SDS-PAGE. This molecular species comprises the postfusion 6-helix bundle, assembled from the heptad repeats 1 and 2, since its formation could be inhibited in the presence of a heptad-repeat-derived peptide that prevents completion of the conformational transition (Matsuyama and Taguchi, 2009). Addition of the S230 Fab (Figure 7A) or the ACE2 ectodomain (Figure 7B) to SARS-CoV S-pseudotyped MLV in the presence of trypsin led to the formation of a proteinase-K-resistant band migrating at approximately 55 kDa, thereby demonstrating that both the antibody and the natural receptor promoted S fusogenic conformational changes in the context of a membrane-embedded full-length S.

Our negative-staining EM findings suggest that ACE2 bound to the SARS-CoV S trimer with a lower affinity than S230 (Figures 6A–6I). Since binding of ACE2 to the isolated B domain was

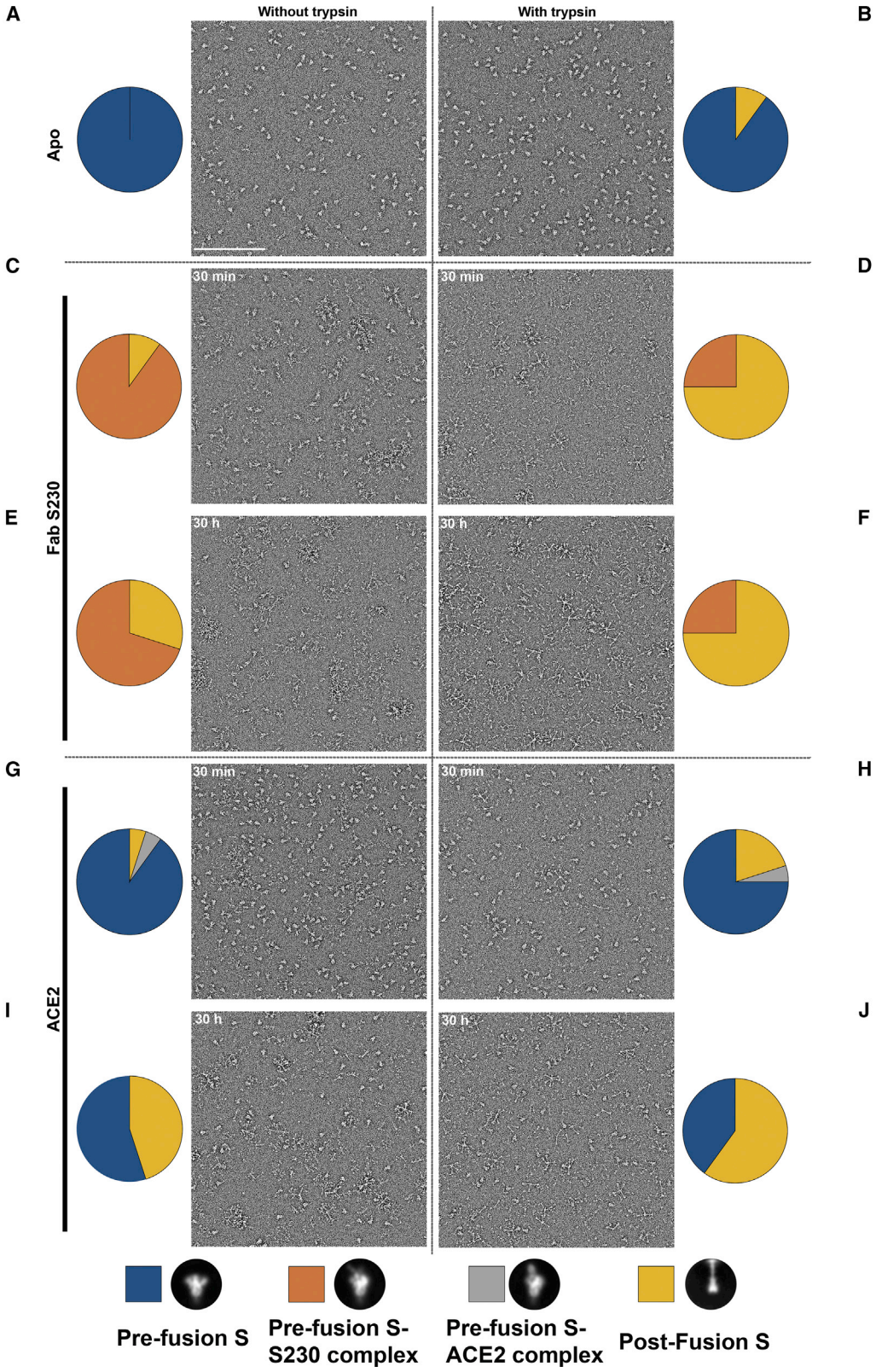

(legend on next page)

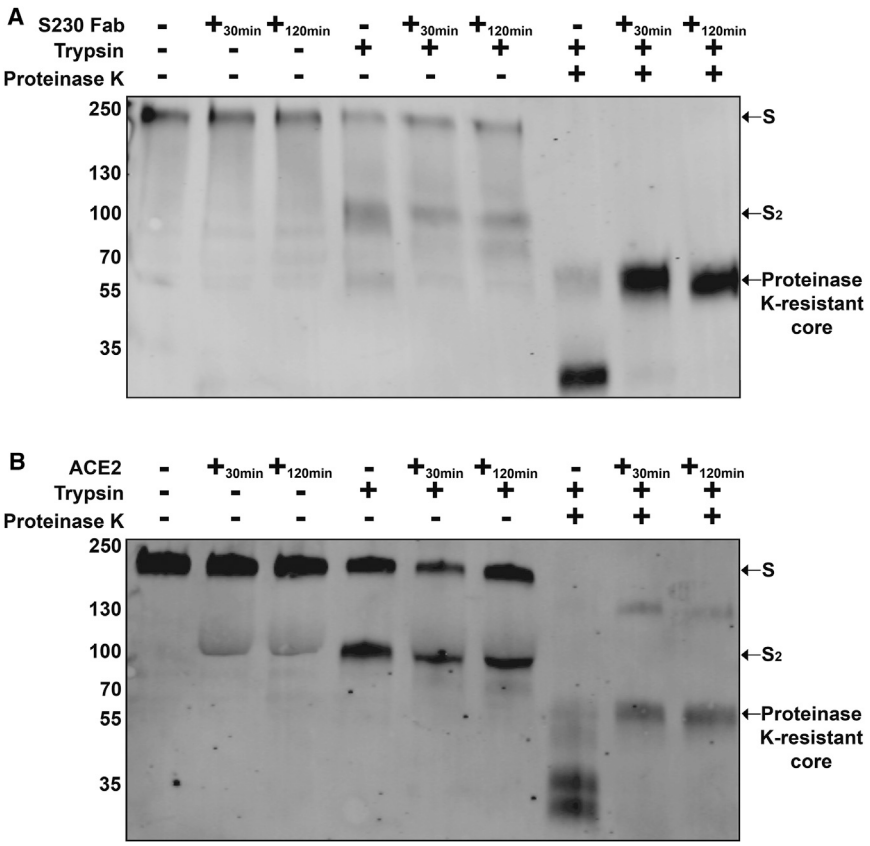

Figure 7. ACE2 or S230-Mediated Refolding of the Full-Length Membrane-Embedded SARS-CoV S Trimer Visualized by Western Blotting

(A and B) The effect of 0.5 μM S230 Fab (A) or of 10 μM ACE2 ectodomain (B) on the conformational state of the full-length SARS-CoV S trimer embedded in the membrane of infectious MLV pseudovirus was probed by western blotting using an anti-SARS-CoV S_2 polyclonal antibody. Refolding to the postfusion conformation was detected by the appearance of a proteinase-K-resistant band migrating at approximately 55 kDa (Matsuyama and Taguchi, 2009). Trypsin was used at 5 μg/mL and proteinase K at 10μg/mL. Digestion experiments and western blots were performed in triplicates, and a representative result is shown for each of them.

reported to have an equilibrium dissociation constant (K_D) in the nanomolar range (Li et al., 2005c), one would expect that full saturation should occur rapidly in the conditions of our experiments (100-fold concentration excess over the K_D). Previous reports, however, suggested a lower affinity of the full-length S trimer, relative to the isolated B domain, for ACE2 (Kirchdoerfer et al., 2018; Matsuyama and Taguchi, 2009; Song et al., 2018). We propose that the conformational landscape of the B domains in the context of the SARS-CoV S trimer, sampling open and closed conformations, decreases the apparent binding affinity for ACE2 and S230 due to masking of their binding sites in the closed state. A similar effect has previously been described for ubiquitin (Michielssens et al., 2014). The higher binding affinity of S230 for SARS-CoV S, compared to ACE2 (Figure S7), resulted in increased complex formation, which explains the more efficient Fab-mediated membrane fusion activation compared to the receptor (Figures 6C–6J and S6).

LCA60 could interact with all possible B domain states. In contrast, S230 binding was restricted to partially or fully open B domains and promoted S fusogenic conformational changes in a way reminiscent of the natural receptor, ACE2. These outcomes indicate that S triggering could work through a ratcheting mechanism involving sequential binding of a receptor molecule to each of the RBM, which in turn traps the B domains in the open conformation. Opening of the B domains releases the constraints imposed on the fusion machinery, thereby allowing the S trimer to refold and fuse the viral and host membranes.

DISCUSSION

Both LCA60 and S230 bind to epitopes partially overlapping with the RBM on the B domain and in turn block attachment to DPP4 or ACE2, respectively, via a competitive mechanism. Moreover, S230 (or ACE2) binding triggered the SARS-CoV S transition to the postfusion conformation. This finding is an unprecedented example of functional mimicry, whereby an antibody activates membrane fusion by recapitulating the action of the receptor. It remains to be investigated whether binding of S230 triggers virus-cell fusion when particles are bound to the surface of cells.

Comparison of the binding modes of LCA60 and S230 with those of DPP4 and ACE2 provides a framework to understand the unique mechanism of coronavirus-membrane-fusion activation. Opening of each of the three B domains reduces the

Figure 6. S230- or ACE2-Mediated Refolding of SARS-CoV S Visualized by Negative Staining EM

(A–J) The effect of Fab S230 (C–F) or of the ACE2 ectodomain (G–J) on the conformational state of the wild-type SARS-CoV S ectodomain trimer was analyzed using single-particle EM of negatively stained samples. Estimates of the fraction of particles corresponding to each state are represented as pie charts based on the number of particle images clustered in each group after reference-free 2D classification. Only pre-fusion and postfusion conformations were included in the calculations, and the results are rendered using bins with a minimal width of 5%. 1.6 μg/mL trypsin was used for (B), (D), (F), (H), and (J). Time points shown at 30 min (C–D and G–H) or 30 h (E, F, I, and J). Representative 2D class averages corresponding to the different states discussed are shown at the bottom. See also Figures S5, S6, and S7.

number of interactions between the S_1 and S_2 subunits and specifically releases the constraints imposed on the heptad-repeat 1-central helix hairpin, which is known to completely refold during the membrane fusion process (Walls et al., 2017). The 660-Å^2 decrease in buried surface area at the interface between the S_1 and S_2 subunits upon opening of the three B domains destabilizes the pre-fusion state and increases its probability of refolding, as observed upon complex formation with ACE2 or S230. Proteolytic activation is likely required to ensure that S glycoproteins will work in synergy, with proper spatial and temporal coordination, to drive fusion of the viral and host membranes. The large number of S glycoproteins decorating the surface of coronaviruses suggests that multiple trimers work in concert for formation of a fusion pore. We expect this activation mechanism to hold true for all coronaviruses using domain B for interacting with their proteinaceous receptor. We view the S_1 subunit as a molecular chaperone, stabilizing the prefusion state of the fusion machinery, and coordinating receptor binding with membrane fusion. In summary, coronaviruses appear to have evolved a fine-tuned balance between masking of the RBM, to limit neutralization by the humoral host immune response, and their necessary exposure, to enable receptor recognition and infection of host cells.

STAR★METHODS

Detailed methods are provided in the online version of this paper and include the following:

- KEY RESOURCES TABLE
- CONTACT FOR REAGENT AND RESOURCE SHARING
- EXPERIMENTAL MODEL AND SUBJECT DETAILS
  - Cell lines
- METHOD DETAILS
  - Construct design
  - Protein expression and purification
  - Pseudovirus production
  - MERS-CoV production
  - MERS-CoV S/LCA60 complex formation
  - SARS-CoV S/S230 complex formation
  - Cryo-EM data collection
  - CryoEM data processing of MERSCoV S/LCA60
  - CryoEM data processing of SARS-CoV S/S230
  - CryoEM Model building and analysis
  - Mass spectrometry
  - SEC-MALS
  - Biolayer interferometry
- QUANTIFICATION AND STATISTICAL ANALYSIS
- DATA AND SOFTWARE AVAILABILITY

SUPPLEMENTAL INFORMATION

Supplemental Information includes seven figures and five tables and can be found with this article online at https://doi.org/10.1016/j.cell.2018.12.028.

ACKNOWLEDGMENTS

We are grateful to Thomas Hinds and Ning Zheng for assistance with the crystallization robot and BLI device; to Jerome Cattin-Ortolà, Irini Topalidou, and Michael Ailion for assistance with western blotting; and to Michelle Chen (Wyatt technology) for her help with the light scattering experiments. This study was supported by the National Institute of General Medical Sciences (R01GM120553, D.V.), the National Institute of Allergy and Infectious Diseases (HHSN272201700059C, D.V.), a Pew Biomedical Scholars Award (D.V.), an Investigators in the Pathogenesis of Infectious Disease Award from the Burroughs Wellcome Fund (D.V.), the Netherlands Organisation for Scientific Research (Rubicon 019.2015.2.310.006, J.S.), the European Molecular Biology Organization (ALTF933-2015, J.S.), the Zoonoses Anticipation and Preparedness Initiative (IMI115760, F.A.R.), the Pasteur Institute (M.A.T. and F.A.R.), the Centre National de la Recherche Scientifique (F.A.R.), the LabEx Integrative Biology of Emerging Infectious Diseases (F.A.R.), the University of Washington Arnold and Mabel Beckman CryoEM Center and Proteomics Resource (UWPR95794), and the beamline 5.0.1 at the Advanced Light Source at Lawrence Berkley National Laboratory.

AUTHOR CONTRIBUTIONS

A.C.W., X.X., J.S., Y.-J.P., and D.V. designed the experiments. A.C.W., X.X., M.A.T., and E.C. designed, expressed, and purified the proteins. A.C.W., X.X., J.Q., and D.V. performed cryo-EM sample preparation, data collection, processing, and built and refined the atomic models. A.C.W. and Y.-J.P. crystallized the Fabs. Y.-J.P. and D.V. processed the diffraction datasets and built and refined the atomic models. A.C.W., X.X., and J.S. performed the MS experiments. A.C.W. and X.X. performed all binding assays. R.G. produced MERS-CoV isolates. M.D., A.L., M.Z., and D.C. provided key reagents. A.C.W., X.X., Y.-J.P. M.A.T., J.S., F.A.R., D.C., and D.V. analyzed the data. A.C.W., X.X., and D.V. prepared the manuscript with input from all authors.

DECLARATION OF INTERESTS

A.L. is the scientific founder and shareholder of Humabs BioMed. D.C. is currently Chief Scientific Officer of Humabs Biomed. The other authors declare no competing financial interests.

Received: July 19, 2018
Revised: October 29, 2018
Accepted: December 17, 2018
Published: January 31, 2019

REFERENCES

Adams, P.D., Afonine, P.V., Bunkóczi, G., Chen, V.B., Davis, I.W., Echols, N., Headd, J.J., Hung, L.-W., Kapral, G.J., Gross-Kunstleve, R.W., et al. (2010). PHENIX: a comprehensive Python-based system for macromolecular structure solution. Acta Crystallogr. D Biol. Crystallogr *66*, 213–221.

Agirre, J., Iglesias-Fernández, J., Rovira, C., Davies, C.J., Wilson, K.S., and Cowtan, K.D. (2015). Privateer: software for the conformational validation of carbohydrate structures. Nat. Struct. Mol. Biol. *22*, 833–834.

Belouzard, S., Chu, V.C., and Whittaker, G.R. (2009). Activation of the SARS coronavirus spike protein via sequential proteolytic cleavage at two distinct sites. Proc. Natl. Acad. Sci. USA *106*, 5871–5876.

Bern, M., Kil, Y.J., and Becker, C. (2012). Byonic: advanced peptide and protein identification software. Curr. Protoc. Bioinformatics *Chapter 13*, Unit 13.20.

Blanc, E., Roversi, P., Vonrhein, C., Flensburg, C., Lea, S.M., and Bricogne, G. (2004). Refinement of severely incomplete structures with maximum likelihood in BUSTER-TNT. Acta Crystallogr. D Biol. Crystallogr *60*, 2210–2221.

Brown, A., Long, F., Nicholls, R.A., Toots, J., Emsley, P., and Murshudov, G. (2015). Tools for macromolecular model building and refinement into electron cryo-microscopy reconstructions. Acta Crystallogr. D Biol. Crystallogr. *71*, 136–153.

Burkard, C., Verheije, M.H., Wicht, O., van Kasteren, S.I., van Kuppeveld, F.J., Haagmans, B.L., Pelkmans, L., Rottier, P.J., Bosch, B.J., and de Haan, C.A. (2014). Coronavirus cell entry occurs through the endo-/lysosomal pathway in a proteolysis-dependent manner. PLoS Pathog. *10*, e1004502.

Chen, V.B., Arendall, W.B., 3rd, Headd, J.J., Keedy, D.A., Immormino, R.M., Kapral, G.J., Murray, L.W., Richardson, J.S., and Richardson, D.C. (2010). MolProbity: all-atom structure validation for macromolecular crystallography. Acta Crystallogr. D Biol. Crystallogr. *66*, 12–21.

Chen, S., McMullan, G., Faruqi, A.R., Murshudov, G.N., Short, J.M., Scheres, S.H., and Henderson, R. (2013). High-resolution noise substitution to measure overfitting and validate resolution in 3D structure determination by single particle electron cryomicroscopy. Ultramicroscopy *135*, 24–35.

Corti, D., Zhao, J., Pedotti, M., Simonelli, L., Agnihothram, S., Fett, C., Fernandez-Rodriguez, B., Foglierini, M., Agatic, G., Vanzetta, F., et al. (2015). Prophylactic and postexposure efficacy of a potent human monoclonal antibody against MERS coronavirus. Proc. Natl. Acad. Sci. USA *112*, 10473–10478.

Cowtan, K. (2006). The Buccaneer software for automated model building. 1. Tracing protein chains. Acta Crytallogr. D Biol. Crystallogr *62*, 1002–1011.

Du, L., Tai, W., Yang, Y., Zhao, G., Zhu, Q., Sun, S., Liu, C., Tao, X., Tseng, C.K., Perlman, S., et al. (2016). Introduction of neutralizing immunogenicity index to the rational design of MERS coronavirus subunit vaccines. Nat. Commun. *7*, 13473.

Emsley, P., Lohkamp, B., Scott, W.G., and Cowtan, K. (2010). Features and development of Coot. Acta Crystallogr. D Biol. Crystallogr. *66*, 486–501.

Evans, P.R., and Murshudov, G.N. (2013). How good are my data and what is the resolution? Acta Crystallogr. D Biol. Crystallogr. *69*, 1204–1214.

Frenz, B., Rämisch, S., Borst, A.J., Walls, A.C., Adolf-Bryfogle, J., Schief, W.R., Veesler, D., and DiMaio, F. (2019). Automatically fixing errors in glycoprotein structures with Rosetta. Structure *27*, 134–139.e3.

Frese, C.K., Zhou, H., Taus, T., Altelaar, A.F., Mechtler, K., Heck, A.J., and Mohammed, S. (2013). Unambiguous phosphosite localization using electron-transfer/higher-energy collision dissociation (EThcD). J. Proteome Res. *12*, 1520–1525.

Ge, X.Y., Li, J.L., Yang, X.L., Chmura, A.A., Zhu, G., Epstein, J.H., Mazet, J.K., Hu, B., Zhang, W., Peng, C., et al. (2013). Isolation and characterization of a bat SARS-like coronavirus that uses the ACE2 receptor. Nature *503*, 535–538.

Goddard, T.D., Huang, C.C., and Ferrin, T.E. (2007). Visualizing density maps with UCSF Chimera. J. Struct. Biol. *157*, 281–287.

Goddard, T.D., Huang, C.C., Meng, E.C., Pettersen, E.F., Couch, G.S., Morris, J.H., and Ferrin, T.E. (2018). UCSF ChimeraX: Meeting modern challenges in visualization and analysis. Protein Sci. *27*, 14–25.

Gui, M., Song, W., Zhou, H., Xu, J., Chen, S., Xiang, Y., and Wang, X. (2017). Cryo-electron microscopy structures of the SARS-CoV spike glycoprotein reveal a prerequisite conformational state for receptor binding. Cell Res. *27*, 119–129.

Haagmans, B.L., Al Dhahiry, S.H., Reusken, C.B., Raj, V.S., Galiano, M., Myers, R., Godeke, G.J., Jonges, M., Farag, E., Diab, A., et al. (2014). Middle East respiratory syndrome coronavirus in dromedary camels: an outbreak investigation. Lancet Infect. Dis. *14*, 140–145.

Hu, B., Zeng, L.P., Yang, X.L., Ge, X.Y., Zhang, W., Li, B., Xie, J.Z., Shen, X.R., Zhang, Y.Z., Wang, N., et al. (2017). Discovery of a rich gene pool of bat SARS-related coronaviruses provides new insights into the origin of SARS coronavirus. PLoS Pathog. *13*, e1006698.

Kabsch, W. (2010). Xds. Acta Crystallogr. D Biol. Crystallogr. *66*, 125–132.

Kimanius, D., Forsberg, B.O., Scheres, S.H., and Lindahl, E. (2016). Accelerated cryo-EM structure determination with parallelisation using GPUs in RELION-2. eLife *5*.

Kirchdoerfer, R.N., Cottrell, C.A., Wang, N., Pallesen, J., Yassine, H.M., Turner, H.L., Corbett, K.S., Graham, B.S., McLellan, J.S., and Ward, A.B. (2016). Pre-fusion structure of a human coronavirus spike protein. Nature *531*, 118–121.

Kirchdoerfer, R.N., Wang, N., Pallesen, J., Wrapp, D., Turner, H.L., Cottrell, C.A., Corbett, K.S., Graham, B.S., McLellan, J.S., and Ward, A.B. (2018). Stabilized coronavirus spikes are resistant to conformational changes induced by receptor recognition or proteolysis. Sci. Rep. *8*, 15701.

Krissinel, E., and Henrick, K. (2007). Inference of macromolecular assemblies from crystalline state. J. Mol. Biol. *372*, 774–797.

Krokhin, O., Li, Y., Andonov, A., Feldmann, H., Flick, R., Jones, S., Stroeher, U., Bastien, N., Dasuri, K.V., Cheng, K., et al. (2003). Mass spectrometric characterization of proteins from the SARS virus: a preliminary report. Mol. Cell. Proteomics *2*, 346–356.

Lander, G.C., Stagg, S.M., Voss, N.R., Cheng, A., Fellmann, D., Pulokas, J., Yoshioka, C., Irving, C., Mulder, A., Lau, P.W., et al. (2009). Appion: an integrated, database-driven pipeline to facilitate EM image processing. J. Struct. Biol. *166*, 95–102.

Li, W., Moore, M.J., Vasilieva, N., Sui, J., Wong, S.K., Berne, M.A., Somasundaran, M., Sullivan, J.L., Luzuriaga, K., Greenough, T.C., et al. (2003). Angiotensin-converting enzyme 2 is a functional receptor for the SARS coronavirus. Nature *426*, 450–454.

Li, F., Li, W., Farzan, M., and Harrison, S.C. (2005a). Structure of SARS coronavirus spike receptor-binding domain complexed with receptor. Science *309*, 1864–1868.

Li, W., Shi, Z., Yu, M., Ren, W., Smith, C., Epstein, J.H., Wang, H., Crameri, G., Hu, Z., Zhang, H., et al. (2005b). Bats are natural reservoirs of SARS-like coronaviruses. Science *310*, 676–679.

Li, W., Zhang, C., Sui, J., Kuhn, J.H., Moore, M.J., Luo, S., Wong, S.K., Huang, I.C., Xu, K., Vasilieva, N., et al. (2005c). Receptor and viral determinants of SARS-coronavirus adaptation to human ACE2. EMBO J. *24*, 1634–1643.

Lu, G., Hu, Y., Wang, Q., Qi, J., Gao, F., Li, Y., Zhang, Y., Zhang, W., Yuan, Y., Bao, J., et al. (2013). Molecular basis of binding between novel human coronavirus MERS-CoV and its receptor CD26. Nature *500*, 227–231.

MacLean, B., Tomazela, D.M., Shulman, N., Chambers, M., Finney, G.L., Frewen, B., Kern, R., Tabb, D.L., Liebler, D.C., and MacCoss, M.J. (2010). Skyline: an open source document editor for creating and analyzing targeted proteomics experiments. Bioinformatics *26*, 966–968.

Matsuyama, S., and Taguchi, F. (2009). Two-step conformational changes in a coronavirus envelope glycoprotein mediated by receptor binding and proteolysis. J. Virol. *83*, 11133–11141.

McCoy, A.J., Oeffner, R.D., Millan, C., Sammito, M., Uson, I., and Read, R.J. (2018). Gyre and gimble: a maximum-likelihood replacement for Patterson correlation refinement. Acta. Crystallogr. D Struct. Biol. *74*, 279–289.

McCoy, L.E., van Gils, M.J., Ozorowski, G., Messmer, T., Briney, B., Voss, J.E., Kulp, D.W., Macauley, M.S., Sok, D., Pauthner, M., et al. (2016). Holes in the Glycan Shield of the Native HIV Envelope Are a Target of Trimer-Elicited Neutralizing Antibodies. Cell Rep. *16*, 2327–2338.

Memish, Z.A., Mishra, N., Olival, K.J., Fagbo, S.F., Kapoor, V., Epstein, J.H., Alhakeem, R., Durosinloun, A., Al Asmari, M., Islam, A., et al. (2013). Middle East respiratory syndrome coronavirus in bats, Saudi Arabia. Emerg. Infect. Dis. *19*, 1819–1823.

Menachery, V.D., Yount, B.L., Jr., Debbink, K., Agnihothram, S., Gralinski, L.E., Plante, J.A., Graham, R.L., Scobey, T., Ge, X.Y., Donaldson, E.F., et al. (2015). A SARS-like cluster of circulating bat coronaviruses shows potential for human emergence. Nat. Med. *21*, 1508–1513.

Menachery, V.D., Yount, B.L., Jr., Sims, A.C., Debbink, K., Agnihothram, S.S., Gralinski, L.E., Graham, R.L., Scobey, T., Plante, J.A., Royal, S.R., et al. (2016). SARS-like WIV1-CoV poised for human emergence. Proc. Natl. Acad. Sci. USA *113*, 3048–3053.

Michielssens, S., Peters, J.H., Ban, D., Pratihar, S., Seeliger, D., Sharma, M., Giller, K., Sabo, T.M., Becker, S., Lee, D., et al. (2014). A designed conformational shift to control protein binding specificity. Angew. Chem. Int. Ed. Engl. *53*, 10367–10371.

Millet, J.K., and Whittaker, G.R. (2014). Host cell entry of Middle East respiratory syndrome coronavirus after two-step, furin-mediated activation of the spike protein. Proc. Natl. Acad. Sci. USA *111*, 15214–15219.

Millet, J.K., and Whittaker, G.R. (2016). Murine Leukemia Virus (MLV)-based Coronavirus Spike-pseudotyped Particle Production and Infection. Biol. Protoc. *6*.otherMillet and Whittaker *2016*.

Ng, M.L., Tan, S.H., See, E.E., Ooi, E.E., and Ling, A.E. (2003). Proliferative growth of SARS coronavirus in Vero E6 cells. J. Gen. Virol. *84*, 3291–3303.

Nkolola, J.P., Bricault, C.A., Cheung, A., Shields, J., Perry, J., Kovacs, J.M., Giorgi, E., van Winsen, M., Apetri, A., Brinkman-van der Linden, E.C., et al. (2014). Characterization and immunogenicity of a novel mosaic M HIV-1 gp140 trimer. J. Virol. *88*, 9538–9552.

Pallesen, J., Wang, N., Corbett, K.S., Wrapp, D., Kirchdoerfer, R.N., Turner, H.L., Cottrell, C.A., Becker, M.M., Wang, L., Shi, W., et al. (2017). Immunogenicity and structures of a rationally designed prefusion MERS-CoV spike antigen. Proc. Natl. Acad. Sci. USA *114*, E7348–E7357.

Park, J.E., Li, K., Barlan, A., Fehr, A.R., Perlman, S., McCray, P.B., Jr., and Gallagher, T. (2016). Proteolytic processing of Middle East respiratory syndrome coronavirus spikes expands virus tropism. Proc. Natl. Acad. Sci. USA *113*, 12262–12267.

Pettersen, E.F., Goddard, T.D., Huang, C.C., Couch, G.S., Greenblatt, D.M., Meng, E.C., and Ferrin, T.E. (2004). UCSF Chimera--a visualization system for exploratory research and analysis. J. Comput. Chem. *25*, 1605–1612.

Punjani, A., Rubinstein, J.L., Fleet, D.J., and Brubaker, M.A. (2017). cryoSPARC: algorithms for rapid unsupervised cryo-EM structure determination. Nat. Methods *14*, 290–296.

Raj, V.S., Mou, H., Smits, S.L., Dekkers, D.H., Müller, M.A., Dijkman, R., Muth, D., Demmers, J.A., Zaki, A., Fouchier, R.A., et al. (2013). Dipeptidyl peptidase 4 is a functional receptor for the emerging human coronavirus-EMC. Nature *495*, 251–254.

Ritchie, G., Harvey, D.J., Feldmann, F., Stroeher, U., Feldmann, H., Royle, L., Dwek, R.A., and Rudd, P.M. (2010). Identification of N-linked carbohydrates from severe acute respiratory syndrome (SARS) spike glycoprotein. Virology *399*, 257–269.

Rockx, B., Corti, D., Donaldson, E., Sheahan, T., Stadler, K., Lanzavecchia, A., and Baric, R. (2008). Structural basis for potent cross-neutralizing human monoclonal antibody protection against lethal human and zoonotic severe acute respiratory syndrome coronavirus challenge. J. Virol. *82*, 3220–3235.

Rosenthal, P.B., and Henderson, R. (2003). Optimal determination of particle orientation, absolute hand, and contrast loss in single-particle electron cryomicroscopy. J. Mol. Biol. *333*, 721–745.

Rossen, J.W., de Beer, R., Godeke, G.J., Raamsman, M.J., Horzinek, M.C., Vennema, H., and Rottier, P.J. (1998). The viral spike protein is not involved in the polarized sorting of coronaviruses in epithelial cells. J. Virol. *72*, 497–503.

Scharf, L., Wang, H., Gao, H., Chen, S., McDowall, A.W., and Bjorkman, P.J. (2015). Broadly Neutralizing Antibody 8ANC195 Recognizes Closed and Open States of HIV-1 Env. Cell *162*, 1379–1390.

Scheres, S.H., and Chen, S. (2012). Prevention of overfitting in cryo-EM structure determination. Nat. Methods *9*, 853–854.

Shang, J., Zheng, Y., Yang, Y., Liu, C., Geng, Q., Tai, W., Du, L., Zhou, Y., Zhang, W., and Li, F. (2017). Cryo-Election Microscopy Structure of Porcine Deltacoronavirus Spike Protein in the Prefusion State. J. Virol. *92*.

Shang, J., Zheng, Y., Yang, Y., Liu, C., Geng, Q., Luo, C., Zhang, W., and Li, F. (2018). Cryo-EM structure of infectious bronchitis coronavirus spike protein reveals structural and functional evolution of coronavirus spike proteins. PLoS Pathog. *14*, e1007009.

Snijder, J., Ortego, M.S., Weidle, C., Stuart, A.B., Gray, M.D., McElrath, M.J., Pancera, M., Veesler, D., and McGuire, A.T. (2018). An Antibody Targeting the Fusion Machinery Neutralizes Dual-Tropic Infection and Defines a Site of Vulnerability on Epstein-Barr Virus. Immunity *48*, 799–811.

Song, W., Gui, M., Wang, X., and Xiang, Y. (2018). Cryo-EM structure of the SARS coronavirus spike glycoprotein in complex with its host cell receptor ACE2. PLoS Pathog. *14*, e1007236.

Stertz, S., Reichelt, M., Spiegel, M., Kuri, T., Martínez-Sobrido, L., García-Sastre, A., Weber, F., and Kochs, G. (2007). The intracellular sites of early replication and budding of SARS-coronavirus. Virology *361*, 304–315.

Stewart-Jones, G.B., Soto, C., Lemmin, T., Chuang, G.Y., Druz, A., Kong, R., Thomas, P.V., Wagh, K., Zhou, T., Behrens, A.J., et al. (2016). Trimeric HIV-1-Env Structures Define Glycan Shields from Clades A, B, and G. Cell *165*, 813–826.

Struwe, W.B., Chertova, E., Allen, J.D., Seabright, G.E., Watanabe, Y., Harvey, D.J., Medina-Ramirez, M., Roser, J.D., Smith, R., Westcott, D., et al. (2018). Site-Specific Glycosylation of Virion-Derived HIV-1 Env Is Mimicked by a Soluble Trimeric Immunogen. Cell Rep *24*, 1958–1966.

Suloway, C., Pulokas, J., Fellmann, D., Cheng, A., Guerra, F., Quispe, J., Stagg, S., Potter, C.S., and Carragher, B. (2005). Automated molecular microscopy: the new Leginon system. J. Struct. Biol. *151*, 41–60.

Traggiai, E., Becker, S., Subbarao, K., Kolesnikova, L., Uematsu, Y., Gismondo, M.R., Murphy, B.R., Rappuoli, R., and Lanzavecchia, A. (2004). An efficient method to make human monoclonal antibodies from memory B cells: potent neutralization of SARS coronavirus. Nat. Med. *10*, 871–875.

Vagin, A.A., Steiner, R.A., Lebedev, A.A., Potterton, L., McNicholas, S., Long, F., and Murshudov, G.N. (2004). REFMAC5 dictionary: organization of prior chemical knowledge and guidelines for its use. Acta. Crystallogr. D Biol. Crystallogr *60*, 2184–2195.

Veesler, D., Blangy, S., Siponen, M., Vincentelli, R., Cambillau, C., and Sciara, G. (2009). Production and biophysical characterization of the CorA transporter from Methanosarcina mazei. Anal. Biochem. *388*, 115–121.

Voss, N.R., Yoshioka, C.K., Radermacher, M., Potter, C.S., and Carragher, B. (2009). DoG Picker and TiltPicker: software tools to facilitate particle selection in single particle electron microscopy. J. Struct. Biol. *166*, 205–213.

Walls, A.C., Tortorici, M.A., Bosch, B.J., Frenz, B., Rottier, P.J.M., DiMaio, F., Rey, F.A., and Veesler, D. (2016a). Cryo-electron microscopy structure of a coronavirus spike glycoprotein trimer. Nature *531*, 114–117.

Walls, A.C., Tortorici, M.A., Frenz, B., Snijder, J., Li, W., Rey, F.A., DiMaio, F., Bosch, B.J., and Veesler, D. (2016b). Glycan shield and epitope masking of a coronavirus spike protein observed by cryo-electron microscopy. Nat. Struct. Mol. Biol. *23*, 899–905.

Walls, A.C., Tortorici, M.A., Snijder, J., Xiong, X., Bosch, B.-J., Rey, F.A., and Veesler, D. (2017). Tectonic conformational changes of a coronavirus spike glycoprotein promote membrane fusion. Proc. Natl. Acad. Sci. USA *114*, 11157–11162.

Wang, M., Yan, M., Xu, H., Liang, W., Kan, B., Zheng, B., Chen, H., Zheng, H., Xu, Y., Zhang, E., et al. (2005). SARS-CoV infection in a restaurant from palm civet. Emerg. Infect. Dis. *11*, 1860–1865.

Wang, Q., Qi, J., Yuan, Y., Xuan, Y., Han, P., Wan, Y., Ji, W., Li, Y., Wu, Y., Wang, J., et al. (2014). Bat origins of MERS-CoV supported by bat coronavirus HKU4 usage of human receptor CD26. Cell Host Microbe *16*, 328–337.

Wang, R.Y., Song, Y., Barad, B.A., Cheng, Y., Fraser, J.S., and DiMaio, F. (2016). Automated structure refinement of macromolecular assemblies from cryo-EM maps using Rosetta. eLife *5*.

Watanabe, Y., Raghwani, J., Allen, J.D., Seabright, G.E., Li, S., Moser, F., Huiskonen, J.T., Strecker, T., Bowden, T.A., and Crispin, M. (2018). Structure of the Lassa virus glycan shield provides a model for immunological resistance. Proc. Natl. Acad. Sci. USA *115*, 7320–7325.

Xiong, X., Tortorici, M.A., Snijder, J., Yoshioka, C., Walls, A.C., Li, W., McGuire, A.T., Rey, F.A., Bosch, B.J., and Veesler, D. (2017). Glycan shield and fusion activation of a deltacoronavirus spike glycoprotein fine-tuned for enteric infections. J. Virol.

Yang, Y., Liu, C., Du, L., Jiang, S., Shi, Z., Baric, R.S., and Li, F. (2015). Two Mutations Were Critical for Bat-to-Human Transmission of Middle East Respiratory Syndrome Coronavirus. J. Virol. *89*, 9119–9123.

Yuan, Y., Cao, D., Zhang, Y., Ma, J., Qi, J., Wang, Q., Lu, G., Wu, Y., Yan, J., Shi, Y., et al. (2017). Cryo-EM structures of MERS-CoV and SARS-CoV spike glycoproteins reveal the dynamic receptor binding domains. Nat. Commun. *8*, 15092.

Zhang, K. (2016). Gctf: Real-time CTF determination and correction. J. Struct. Biol. *193*, 1–12.

Zhang, H., Wang, G., Li, J., Nie, Y., Shi, X., Lian, G., Wang, W., Yin, X., Zhao, Y., Qu, X., et al. (2004). Identification of an antigenic determinant

on the S2 domain of the severe acute respiratory syndrome coronavirus spike glycoprotein capable of inducing neutralizing antibodies. J. Virol. *78*, 6938–6945.

Zheng, S.Q., Palovcak, E., Armache, J.P., Verba, K.A., Cheng, Y., and Agard, D.A. (2017). MotionCor2: anisotropic correction of beam-induced motion for improved cryo-electron microscopy. Nat. Methods *14*, 331–332.

Zivanov, J., Nakane, T., Forsberg, B.O., Kimanius, D., Hagen, W.J., Lindahl, E., and Scheres, S.H. (2018). New tools for automated high-resolution cryo-EM structure determination in RELION-3. eLife *7*.

Zivanov, J., Nakane, T., and Scheres, S.H.W. (2019). A Bayesian approach to beam-induced motion correction in cryo-EM single-particle analysis. IUCrJ *6*, 5–17.

STAR★METHODS

KEY RESOURCES TABLE

REAGENT or RESOURCE	SOURCE	IDENTIFIER
Antibodies		
SARS-CoV S polyclonal antibody	ThermoFisher	Cat# PA1-41385; RRID: AB_1087215 Lot# TI2631279
AlexaFluor680-conjugated AffiniPure Goat Anti Rabbit IgG	JacksonImmuno (Gift from Michael Ailion lab)	Cat# 111-625-144; RRID: AB_2338085 Lot# 114199
Bacterial and Virus Strains		
MERS-EMC/2012	Gift from Bart Haagmans and Ron Fouchier	GenBank: JX869059.2
MERS-England 1	Corti et al., 2015	GenBank: KC164505.2
Chemicals, Peptides, and Recombinant Proteins		
Trypsin	ThermoFisher	Ref# 90057 Lot# TG269188
Chymotrypsin	Sigma-Aldrich	Cat# 9004-07-3
Alphalytic Protease	Sigma-Aldrich	Cat# A6362
AspN Endoproteinase	NEB	Cat# P8104S
EndoH	NEB	Cat# P0702S Lot# 0181603
EndoF3	CalBIOCHEM	Cat# 324727 Lot# 2754801
Proteinase K	ThermoScientific	Cat# EO0491 Lot# 00656887
EDC	ForteBio, Pall	Cat# 18-1033 Lot # SF252306
Sulfo-NHS	ForteBio, Pall	Cat# 18-1067 Lot# R124327
Uranyl Formate	Electron Microscopy Sciences	Cat# 22451 Lot# 150212
Deposited Data		
Raw and Analyzed Mass Spectrometry Data	This Paper	PRIDE: PDX010494
MERS-CoV S2P/LCA60 cryoEM maps	This Paper	EMDB: 0401, 0402
MERS-CoV S2P/LCA60 atomic models	This Paper	PDB: 6NB3, 6NB4
SARS-CoV S 2P/S230 cryoEM maps	This Paper	EMDB: 0403, 0404
SARS-CoV S 2P/S230 atomic models	This Paper	PDB: 6NB6, 6NB7
LCA60 crystal structure	This Paper	PDB: 6NB5
S230 crystal structure	This Paper	PDB: 6NB8
Experimental Models: Cell Lines		
Freestyle HEK293	ThermoFisher	Cat# R79007
HEK293T/17 adherent	Millet and Whittaker, 2016	ATCC CRL-11268
Expi293F	ThermoFisher	Cat# A14527
Vero(C1008)E6 adherent	ECACC General Collection	Cat# 85020206
Recombinant DNA		
pOPING – MERS-CoV S 2P	GeneArt	N/A
pOPING – SARS-CoV S 2P	GeneArt	N/A
pcD5 - ACE2	Raj et al., 2013	N/A
LCA60	Corti et al., 2015	N/A
S230	Rockx et al., 2008	N/A
pcDNA3.1(-) –Full-length wild-type SARS-CoV S	Millet and Whittaker, 2016	N/A
pCMV-murine leukemia virus gag-pol	Millet and Whittaker, 2016	N/A
pTG-Luciferase	Millet and Whittaker, 2016	N/A

(*Continued on next page*)

Continued

REAGENT or RESOURCE	SOURCE	IDENTIFIER
pCAGGS-SARS-CoV-S_1-Fc	Raj et al., 2013	N/A
pCAGGS-MERS-CoV-S_1-Fc	Raj et al., 2013	N/A
Software and Algorithms		
UCSF Chimera	Pettersen et al., 2004	https://www.rbvi.ucsf.edu/chimera/
UCSF ChimeraX	Goddard et al., 2018	https://www.rbvi.ucsf.edu/chimerax/
GCTF	Zhang, 2016	https://www.mrc-lmb.cam.ac.uk/kzhang/Gctf/
COOT	Emsley et al., 2010	https://www2.mrc-lmb.cam.ac.uk/personal/pemsley/coot/
Relion	Zivanov et al., 2018	https://www2.mrc-lmb.cam.ac.uk/relion/index.php?title=Main_Page
Protein Metrics Byonic software	Bern et al., 2012	https://www.proteinmetrics.com/products/byonic/
PHENIX	Adams et al., 2010	http://www.phenix-online.org/
PISA	Krissinel and Henrick, 2007	http://www.ebi.ac.uk/msd-srv/prot_int/pistart.html
Rosetta	Frenz et al., 2019	https://www.rosettacommons.org/software
Leginon	Suloway et al., 2005	http://emg.nysbc.org/redmine/projects/leginon/wiki/Leginon_Homepage
DoG Picker	Voss et al., 2009	http://emg.nysbc.org/redmine/projects/software/wiki/DoGpicker
Privateer	Agirre et al., 2015	http://www.ccp4.ac.uk/html/privateer.html
Buster		https://www.globalphasing.com/buster/
CryoSPARC	Punjani et al., 2017	https://cryosparc.com
REFMAC5	Vagin et al., 2004	http://www.ccp4.ac.uk/html/refmac5
Other		
Octet Red	ForteBio, Pall	https://www.fortebio.com/octet-RED96.html
Amine Reactive 2nd Generation (AR2G) Biosensors	ForteBio, Pall	Part# 18-5092 Lot# 1805262
HisTALON Superflow cartridge	Takara	Cat# 635683 Lot# 1509573A
Superose 6 Increase 10/300	GE Life Sciences	Cat# 29-0915-96 Lot# 10226998
Lacey Formvar/Carbon 400 mesh, Cu Grids	Ted Pella	Prod# 01885-F Lot# 020218

CONTACT FOR REAGENT AND RESOURCE SHARING

Further information and requests for resources and reagents should be directed to and will be fulfilled by the Lead Contact, David Veesler (dveesler@uw.edu).

EXPERIMENTAL MODEL AND SUBJECT DETAILS

Cell lines

HEK293F is a female human embryonic kidney cell line transformed and adapted to grow in suspension (Life Technologies). HEK293F cells were grown in 293FreeStyle expression medium (Life Technologies), cultured at 37°C with 5% CO_2 and 150 rpm. HEK293T/17 is a female human embryonic kidney cell line (ATCC). HEK293T/17 cells were cultured at 37°C with 5% CO2 in flasks with DMEM + 10% FBS + penicillin-streptomycin + 10mM HEPES. Expi293F is a female human embryonic kidney cell line transformed and adapted to grow in suspension (Life Technologies). Expi293F cells were grown in Expi293F expression medium, cultured at 37°C, 5% CO2 and 150 rpm. VeroE6 is a female kidney epithelial cell from African green monkey. VeroE6 cells were grown in serum-free medium (VP-SFM; ThermoFisher) at 37°C and 5% CO_2. Cells lines were not tested for mycoplasma contamination nor authenticated except for the VeroE6 cells.

METHOD DETAILS

Construct design

Genes encoding for the ectodomains of both MERS-CoV and SARS-CoV S were synthesized by GeneArt (ThermoFisher Scientific) and placed into a modified pOPING vector with its original N-terminal mu-phosphatase signal peptide, and an engineered C-terminal extension: SG-R*ENLYFQG (TEV protease site),* GGGSG-YIPEAPRDGQAYVRKDGEWVLLSTFL (foldon trimerization motif), G-HHHHHH (hexa-histidine tag), just upstream of the predicted transmembrane region (YNK for MERS-CoV S and YIK for SARS-CoV S). The MERS-CoV S_1/S_2 furin cleavage site was mutated and both SARS-CoV and MERS-CoV S were stabilized with the 2P mutations (Pallesen et al., 2017). The SARS-CoV S_1 and ACE2 ectodomain constructs were fused to a sequence encoding a thrombin cleavage site and a human Fc fragment at the C-terminal end (kind gifts from Berend-Jan Bosch), as previously described (Raj et al., 2013).

Protein expression and purification

The SARS-CoV S 2P and MERS-CoV S 2P ectodomains were produced in 500mL HEK293F cells grown in suspension using FreeStyle 293 expression medium (Life technologies) at 37°C in a humidified 8% CO2 incubator rotating at 130 rpm The cultures were transfected using 293fectin (ThermoFisher Scientific) with cells grown to a density of 1 million cells per mL and cultivated for three days. The supernatants were harvested and cells resuspended for another three days, yielding two harvests. Clarified supernatants were purified using a 5mL Cobalt affinity column (Takara). Purified protein was filtered or concentrated and flash frozen in Tris-saline (50 mM Tris pH 8.0, 150 mM NaCl) prior to negative staining and cryo-EM analysis. Wild-type SARS-CoV S was expressed in 293F cells and purified the same way as the SARS-CoV S 2P. Wild-type SARS-CoV S was filtered through 0.2 μm filter and the quality of the protein was assessed by negative stain electron microscopy and SDS-PAGE. Wild-type SARS-CoV S was not frozen and was stored at 4°C and used within 7 days of purification.

Expression and purification of human angiotensin-converting enzyme ectodomain (ACE2, residues 1–614) fused to the Fc region of human IgG (hFc) was performed following the protocol previously described for CEACAM1a(Walls et al., 2016a) and cleavage of the Fc fragment was achieved using trypsin or thrombin. SARS-CoV S_1-Fc was produced in 250mL HEK293F cells grown in suspension using FreeStyle 293 expression medium (Life technologies) at 37°C in a humidified 8% CO2 incubator rotating at 130 rpm The cultures were transfected using 293fectin (ThermoFisher Scientific) with cells grown to a density of 1 million cells per mL and cultivated for six days. The supernatant was harvested, clarified and incubated with 0.25mL protein A beads (0.5 mL slurry) (GenScript) overnight. Beads were washed thoroughly with phosphate buffered saline prior to elution with 0.1M glycine pH3.0 which was immediately neutralized with 1M Tris pH8.5. LCA60 and S230 Fabs were expressed using transient transfection of Expi293F cells, purified by affinity chromatography using CaptureSelect CH1-XL column (ThermoFisher), buffer exchanged to phosphate buffer saline using a HiTrap fast desalting column (GE Healthcare) and sterilized through a 0.2 μm filter.

Pseudovirus production

MLV-based SARS-CoV S-pseudotyped were prepared as previously described (Millet and Whittaker, 2016). HEK293T cells were co-transfected with a SARS-CoV S encoding-plasmid, a MLV Gag-Pol packaging construct and the MLV transfer vector encoding a luciferase reporter using the Lipofectamine 2000 transfection reagent (Life Technologies) according to the manufacturer's instructions. Cells were incubated for 5 hours at 37°C with 5% CO_2 with transfection medium. Cells were then washed with DMEM 2X and DMEM containing 10% FBS was added for 12 hours. The cells were washed again 2X with DMEM and were kept in DMEM without FBS for 48 hours (Wang et al., 2014). The supernatants were then harvested and filtered through 0.45-μm membranes.

MERS-CoV production

Virions were purified from the supernatant of infected Vero E6 cells. Cells were infected at 90% confluence at multiplicity of infection of 0.01, in Serum Free Medium (VP-SFM; ThermoFisher Scientific). Cultures were maintained at 37°C, 5% (v/v) CO_2 until 3 days post infection when the culture supernatant was removed. Approximately 50% of cells were rounding, but most remained attached to the growth surface. For virion purification, culture supernatant was clarified by centrifugation at 1,400 g for 10 min then overlaid on a cushion of 20% (w/w) Sucrose in Hanks Buffered Saline solution (HBSS: ThermoFisher Scientific) .Supernatant virions were centrifuged through the cushion at 100,000 g for 90 min at 4°C. Pelleted virions were resuspended in HBSS and disrupted by heating for 10 min at 95°C in 1% (w/v) sodium dodecyl sulfate. All live virus work was undertaken under UK ACDP Containment level 3 conditions.

MERS-CoV S/LCA60 complex formation

Flash frozen MERS-CoV 2P stabilized S at 5mg/mL was incubated in a 1:1.5 molar ratio with LCA60 at 2.3 mg/mL on ice for three hours. Trypsin at 3 μg/mL was added for twenty minutes at 37°C prior to injection over a gel filtration column (Superose 6 10/300 from GE Life Sciences) equilibrated in 20mM Tris pH8.0 and 150mM NaCl. The complex peak fractions were concentrated to 0.5 mg/mL. 3 μL was applied to a glow discharged (20 s at 20 mA) lacey carbon copper grid with a thin layer of evaporated continuous carbon prior to plunge freezing into liquid ethane with a Mark IV vitrobot (ThermoFisher Scientific) using −1 blot force and 2 s blot time at 95% humidity and 25°C.

SARS-CoV S/S230 complex formation

Lacey carbon copper grids were coated with a thin-layer of continuous carbon using a carbon evaporator and glow discharged for 20 s at 20 mA. Flash frozen SARS-CoV 2P stabilized S was diluted to 0.05 mg/mL and 2 μl was applied to the grid and incubated for 1 min. Subsequently, the grid was washed three times in Tris-saline buffer before 2 μL of S230 Fab at 0.02 mg/mL was applied to the grid and incubated for five minutes. The grid was washed again three times with Tris-saline after the Fab incubation and manually blotted prior to plunge freezing into liquid ethane at room temperature.

Cryo-EM data collection

Data were acquired using the Leginon software (Suloway et al., 2005) to control an FEI Titan Krios transmission electron microscope operated at 300 kV and equipped with a Gatan K2 Summit direct detector and Gatan Quantum GIF energy filter, operated in zero-loss mode with a slit width of 20 eV. Automated data collection was carried out using Leginon at a nominal magnification of 105,000x with a pixel size of 0.685 Å. The dose rate was adjusted to 8 counts/pixel/s, and each movie was acquired in super-resolution mode fractionated in 50 frames of 200 ms. For MERS-CoV S/LCA60, 2,400 micrographs were collected in a single session with a defocus range comprised between 0.6 and 3.0 μm. For SARS-CoV S/S230, 5,900 images were collected in a single session with a defocus range comprised between 0.8 and 3.0 μm.

CryoEM data processing of MERSCoV S/LCA60

Movie frame alignment was carried out with MotionCorr2 (Zheng et al., 2017) using a dose weighting of 40 $e^-/Å^2$. The parameters of the microscope contrast-transfer function were estimated with GCTF (Zhang, 2016). Particles were automatically picked with DoGPicker (Voss et al., 2009) through the Appion interface (Lander et al., 2009). Particle images were extracted and processed with Relion3.0 (Kimanius et al., 2016) with a box size of 768 $pixels^2$ binned to 384 $pixels^2$ yielding a pixel size of 1.37Å. Reference free 2D classification was used to parse 240,000 particles from the original 500,000 particle images using Relion3.0. An initial model was generated from PDBID 5W9J with all MERS-CoV S domain B closed and removing the G4 Fab (Pallesen et al., 2017). Relion3.0 3D classification with C1 symmetry was utilized to select the ~126,000 best particles for state 1 and the ~114,000 best particles for state 2. CTF refinement in Relion3.0 was used to refine per-particle defocus values. Particles images from each state were subjected to the Bayesian polishing procedure implemented in Relion3.0 (Zivanov et al., 2018, 2019) and 3D refinement before performing 3D classification, without refining angle and shifts, using soft masks focusing on the B domains and Fabs with a tau factor of 50. 82,000 and 78,000 particles were selected for states 1 and 2, respectively. Particle images from state 1 underwent another round of domain B/LCA60 focused classification to select 54,000 particles used for the final reconstruction. Finally, CryoSPARC non-uniform refinement (Punjani et al., 2017) was used to obtain the final reconstructions at 3.5 and 3.6 Å resolution, respectively, using soft masks excluding the open B domains and bound Fabs. Reported resolutions are based on the gold-standard FSC = 0.143 criterion (Rosenthal and Henderson, 2003; Scheres and Chen, 2012) and Fourier shell correlation curves were corrected for the effects of soft masking by high-resolution noise substitution(Chen et al., 2013). Local resolution estimation, filtering and sharpening was carried out using CryoSPARC. Analysis was carried out using the state 1 structure since the reconstruction is best resolved.

CryoEM data processing of SARS-CoV S/S230

Movie frame alignment was carried out with MotionCorr2 (Zheng et al., 2017) using a dose weighting of 40 $e^-/Å^2$. The parameters of the microscope contrast-transfer function were estimated with GCTF (Zhang, 2016). Particles were automatically picked with DoGPicker (Voss et al., 2009) through the Appion interface (Lander et al., 2009). Particle images were extracted and processed with Relion3.0 (Kimanius et al., 2016) with a box size of 768 $pixels^2$ binned to 72 $pixels^2$ (for 2D classification), 128 $pixels^2$ (for 3D classification) or 384 $pixels^2$ (for 3D refinement, yielding a pixel size of 1.37Å). Two rounds of Relion reference-free 2D classification were used to select ~350,000 particles clustering in well-defined class averages. An initial model was generated from a SARS-CoV S structure with all B domains closed (PDB: 5X58) (Yuan et al., 2017). Relion 3D classification without applying symmetry was utilized to select ~162,000 particle images for state 1 (including numerous conformations of the two bound Fabs as well as partial occupancy) and ~126,000 particle images for state 2 (including numerous conformations of the three bound Fabs as well as partial occupancy). Particle images in each subset were then subsequently subjected to a new round of 3D classification without imposing symmetry and using the same initial model as for the previous round. A subset of ~65,000 particle images from state 1 and ~71,000 particle images from state 2 were selected based on reduced conformational heterogeneity of the bound Fabs (which exhibit a continuum of conformational states) and independently used to run 3D auto-refinements using Relion. Particle images from each state were subjected to the Bayesian polishing procedure implemented in Relion3.0 (Zivanov et al., 2018; Zivanov et al., 2019) and 3D refinement before performing 3D classification, without refining angle and shifts, using soft masks focusing on the B domains and Fabs with a tau factor of 30. ~23,000 and 20,000 particles were selected for states 1 and 2, respectively, based on mobility of the bound Fabs which were less well resolved than SARS-CoV S (especially the S_2 subunit) in the maps. Finally, CryoSPARC non-uniform refinement (Punjani et al., 2017) was used to obtain the final reconstructions at 4.2 Å and 4.5 Å resolution for states 1 and 2, respectively. Reported resolutions are based on the gold-standard FSC = 0.143 criterion (Rosenthal and Henderson, 2003; Scheres and Chen, 2012) and Fourier shell correlation curves were corrected for the effects of soft masking by high-resolution noise substitution (Chen et al., 2013). Local resolution estimation, filtering and sharpening was carried out using CryoSPARC.

CryoEM Model building and analysis

UCSF Chimera (Goddard et al., 2007) and Coot were used to fit atomic models (PDB: 5W9J for MERS and PDB: 5X58 for SARS) into the cryoEM maps. The crystal structure of LCA60 or S230 were also fit into density using UCSF Chimera. The models were subsequently manually rebuilt using Coot (Brown et al., 2015; Emsley et al., 2010). N-linked glycans were hand-built into the density where visible and the models were refined and relaxed using Rosetta (Wang et al., 2016). Glycan refinement relied on a dedicated Rosetta protocol, which uses physically realistic geometries based on prior knowledge of saccharide chemical properties (Frenz et al., 2019), and was aided by using both sharpened and unsharpened maps. Models were analyzed using MolProbity (Chen et al., 2010) and privateer (Agirre et al., 2015). Figures were generated using UCSF ChimeraX (Goddard et al., 2018).

Negative stain electron microscopy

Protein was adsorbed to glow-discharged carbon-coated copper grids for 1 min prior to a 3X wash with water and 2% uranyl formate staining. Micrographs were recorded using the Leginon software (Suloway et al., 2005) on a 100kV FEI Tecnai G2 Spirit with a Gatan Ultrascan 4000 4k x 4k CCD camera at 67,000 nominal magnification. The defocus ranged from 1.0 to 2.0 μm and the pixel size was 1.6 Å. Particles were picked automatically in a reference free manner using DogPicker. Contrast transfer function (CTF) estimation was performed using GCTF (Zhang, 2016). Class averages were generated using Relion2.1 (Kimanius et al., 2016).

Crystallization, data collection and data processing of LCA60 and S230

Fab LCA60 crystals were grown in hanging drop set up with a mosquito at 20°C using 150 nL protein solution and 150 nL mother liquor solution containing 30% (v/v) Jeffamine ED-2001 pH 7.0 and 0.1 M HEPES pH 7.0. The LCA60 dataset was collected at the ALS beamline 5.0.1 and processed to 3.0 Å resolution in space group $P2_1$, with cell dimensions a = 70.72 Å b = 69.57 Å and c = 93.84 Å, using XDS (Kabsch, 2010) and Aimless (Evans and Murshudov, 2013). Fab S230 crystals were grown in hanging drop set up with a mosquito at 20°C using 150 nL protein solution and 150 nL mother liquor solution containing 3.5 M sodium formate pH 7.0. Crystals were cryo-protected using the mother liquor solution supplemented with 30% glycerol. The S230 dataset was collected at the ALS beamline 5.0.1 and processed to 1.5 Å resolution in space group $P2_12_12_1$ using XDS and Aimless. The structures of Fab LCA60 and Fab S230 were solved by molecular replacement using Phaser (McCoy et al., 2018) and homology models as search models. The coordinates were subsequently improved and completed using Buccaneer (Cowtan, 2006) and COOT (Brown et al., 2015; Emsley et al., 2010) and refined with BUSTER-TNT (Blanc et al., 2004) and REFMAC5 (Vagin et al., 2004). Simulated annealing and omit map calculations were performed in Phenix (Adams et al., 2010). The quality of the crystal structures were analyzed using MolProbity (Chen et al., 2010). Crystallographic data collection and refinement statistics are shown in Table S4.

Ligand-induced conformational change analysis using negative staining EM

The wild-type SARS-CoV S ectodomain trimer at 1 mg/mL (7.5 μM spike monomer) was incubated with equimolar amount of Fab S230 or 4-fold molar excess of ACE2 for 30 min or overnight (20-30 hours) on ice. Samples were taken at the end of the incubation and imaged by negative staining EM. The incubation mixtures were also subjected to digestion with trypsin at 1.6 μg/mL at room temperature and reactions were analyzed by SDS-PAGE at different time points. The digestion reaction was stopped by addition of 1.5 mM PMSF after 15 min for imaging by negative staining EM. To visualize the effect of ligand binding on pre-digested wild-type SARS-CoV S ectodomain trimer, the protein at 1 mg/mL was digested with 1.6 μg/mL trypsin for 15 min at room temperature before stopping the reaction using 1.5 mM PMSF. The pre-digested wild-type SARS-CoV S ectodomain trimer was incubated with S230 or ACE2 on ice for 30 min or overnight before negative staining EM imaging.

Ligand-induced conformational change analysis using Western-blotting

SARS-CoV S pseudovirions were thawed and incubated either with an equal volume of buffer, 10 μM of the ACE2 ectodomain or 500 nM S230 Fab for 30 min or 2 hours on ice. Trypsin (5 μg/mL) was then added to these samples for 30 min at 37°C. Subsequently, the samples were supplemented with 10 μg/mL proteinase K for 30 min at 4°C. 6X SDS-PAGE loading buffer was then added to all samples prior to boiling at 95°C for 5 min. Samples were run on a 4%–15% gradient Tris-Glycine Gel (BioRad) and transferred to PVDF membranes. An anti-S_2 SARS-CoV S polyclonal primary antibody (1:1,500 dilution, ThermoFisher) and an Alexa Fluor 680-conjugated goat anti-rabbit secondary antibody (1:20,000 dilution, Jackson Laboratory) were used for Western-blotting. A LI-COR processor was used to develop images.

Mass spectrometry

In solution: MERS-CoV S or SARS-CoV S were either unaltered or subjected to Endo-F and Endo-H deglycosylation treatment. Two microliters of the deglycosylases were allowed to incubate with 20 μg of S for 4-14 hr in 50mM sodium acetate pH 4.4 at 37°C in a 20 μL reaction. 6 μg of S were then incubated in 100mM Tris pH 8.5, 2% sodium deoxycholate, 10mM tris(2-carboxyethyl)phosphine, and 40mM iodoacetamide at 95°C for five minutes and 25°C for thirty minutes in the dark. Denaturated, reduced, and alkylated S (1.6 μg) was then diluted into fresh 50mM Ammonium bicarbonate and incubated for 14 hr at 37°C either with 0.032 μg of trypsin (Sigma Aldrich), chymotrypsin (Sigma Aldrich), trypsin then sequentially chymotrypsin, alpha lytic protease (Sigma), or AspN protease (Pierce). Formic acid was then added to a final concentration of 2% and the samples spun at 14,000 rpm for 20 min and then again for 5 min to precipitate the sodium deoxycholate and collect the peptides from the supernatants. The SARS S digests with trypsin, chymotrypsin and alpha lytic protease were processed in parallel after cotton-enrichment of glycopeptides. Approximately 0.5 mg of cotton wool was packed into 100 μL pipette tips. Glycopeptides were diluted in 80% acetonitrile with 0.1% formic acid and bound to the cotton plug, followed by washing of the cotton plug with 80% acetonitrile with 0.1% formic acid. Glycopeptides were eluted in 0.1% formic acid in water.

In gel: 120 μL of MERS-CoV England1 and EMC2012 virions and 40 μg of purified MERS2P were run on a 4%–15% gradient Tris-Glycine Gel (BioRad). One lane of each sample was loaded with 40 μL while a second lane was loaded with 40 μL, allowed to run for 2 min, and loaded with another 40 μL. The bands were excised and washed with milliQ water and acetonitrile. 1 mg/mL DTT in 50mM ammonium bicarbonate was incubated with the gel pieces at 60°C for 1 hour. Following an acetonitrile wash, 10 mg/mL iodoacetamide in 50mM ammonium bicarbonate was incubated for 30 min at room temperature in darkness. Following extensive washes, either 30 μg/mL trypsin or chymotrypsin in ammonium bicarbonate was incubated with the gel pieces for 1.5 hours on ice. The solution was replaced with ammonium bicarbonate and incubated overnight at 37°C. The supernatant was collected and dried down in a speedvac for 1 hr. The peptides were reconstituted in 40 μL 10% formic acid, 5% DMSO.

Peptide supernatant was collected and between 4 and 8 μL were run on a Orbitrap Fusion Tribrid (ThermoFisher Scientific) mass spectrometer. A 35 cm analytical column and a 3cm trap column filled with ReproSil-Pur C18AQ 5 μm (Dr. Maisch GMBH) beads was used. Nanospray LC-MS/MS was used to separate peptides over a 110-min gradient from 5% to 30% acetonitrile. A positive spray voltage of 2100 was used with an ion transfer tube temperature of 350°C. An electron-transfer/higher energy collision dissociation ion fragmentation scheme was used (Frese et al., 2013). The supplemental higher energy collision dissociation energy was 0.15 for the runs. A resolution setting of 120,000 with an AGC target of $2*10^5$ was used for MS1, and a resolution setting of 30,000 with an AGC target of $1*10^5$ was used for MS2. The data was then analyzed using Byonic (Bern et al., 2012) against a custom database of recombinant coronavirus spike proteins, searching for glycan modifications with 12/24 ppm search windows for MS1/MS2, respectively. The in-solution digestions of the recombinant ectodomain were searched against a custom database of recombinant coronavirus spike proteins, proteases, and common contaminants. The in-gel digestion experiments were first searched against a database comprised of the full MERS-CoV proteome and the full Chlorocebus sabaeus (virus produced in VeroE6 cells) or human proteome (ectodomain produced in HEK293F cells) retrieved from UniProt, with variable N-linked glycosylations omitted from the search to identify background contaminants. The top 16 contaminants were then assembled together with the S sequence into a focused database for the glycopeptide identifications. In all experiments, up to three missed cleavages were permitted using C-terminal cleavage at R/K for trypsin, F/Y/W/M/L for chymotrypsin, R/K/F/Y/W/M/L for trypsin-chymotrypsin, T/A/S/V for alpha lytic protease, and N-terminal cleavage at D for AspN. Carbamidomethylation of cysteine was set as fixed modification, methionine oxidation and carbamidomethylation of lysine as variable common 1, glycan modifications as variable common 2, with a variable common max. parameter of 3. The N-linked glycan databases of Byonic were merged into a single non-redundant set of glycan compositions for the searches. All reported glycopeptides in the Byonic results files were manually inspected for quality of fragment assignments. All glycopeptide identifications were merged into a single non-redundant list per sequon. Glycans were classified based on HexNAc content as high-mannose (2 HexNAc), hybrid (3 HexNAc) or complex (> 3 HexNAc). Byonic search results were exported to mzIdentML format to build a spectral library in Skyline (MacLean et al., 2010) and extract peak areas for individual glycoforms from MS1 scans. The full database of variable N-linked glycan modifications from Byonic was manually added to the Skyline project file in XML format. Byonic search results from in-gel digestions of both virion samples and ectodomain were merged into a single spectral library and manually inspected for quantitation. Reported peak areas were pooled based on the number of HexNAc, Fuc or NeuAc residues to distinguish high-mannose/hybrid/complex glycosylation, fucosylation and sialylation, respectively.

SEC-MALS

30 μl of each sample at 2.5 mg/mL were loaded onto a Vanquish column (ThermoFisher Scientific) with Acquity UPLC protein BEH SEC, 450Å, 2.5 μm, 4.6 mm x 150mm (Waters) and passed through a Wyatt μDAWN coupled to a Wyatt Optilab UT-rEX differential refractive index detector. Data were analyzed using Astra 6 software (Wyatt Technology Corp) to quantify the protein and glycan weight.

Biolayer interferometry

Assays were performed on an Octet Red instrument at 30°C with shaking at 1,000 RPM. ARG2 biosensors were hydrated in water then activated for 300 s with an NHS-EDC solution (ForteBio) prior to amine coupling. 30 μg/mL SARS-S1-Fc was amine coupled to ARG2 (ForteBio) sensors in pH5.0 10mM acetate (ForteBio) respectively for 600 s (4nm shift) and then quenched with 1M ethanolamine for 600 s. A baseline in 25mM Phosphate pH8.0, 150mM NaCl, 1% BSA was collected for 120 s prior to immersing the sensors in a serial dilution of either ACE2 or S230 for 600 s prior to dissociation in buffer for 600 s. ACE2 concentrations used were 1,000 nm, 333 nM, 111 nM, 37 nM, 12.3 nM, and 4.12 nM. S230 concentrations used were 100 nM, 33.3 nM, 11.1 nM, 3.7 nM, 1.23 nM, and 0.412 nM. Curve fitting was performed using a 1:1 binding model and the ForteBio data analysis software. Mean k_{on}, k_{off} values were determined with a global fit applied to all data.

QUANTIFICATION AND STATISTICAL ANALYSIS

Digestion followed by Western-blotting experiments as well as biolayer interferometry assays were performed in triplicates.

DATA AND SOFTWARE AVAILABILITY

The cryoEM maps and atomic models have been deposited at the Electron Microscopy Data Bank and the Protein Data Bank with accession codes EMDB: 0401 and PDB: 6NB3 (MERS-CoV S/LCA60 state 1), EMDB: 0402 and PDB: 6NB4 (MERS-CoV S/LCA60 state 2), EMDB: 0403 and PDB: 6NB6 (SARS-CoV S/S230 state 1), EMDB: 0404 and PDB: 6NB7 (SARS-CoV S/S230 state 2). The crystal structures have been deposited in the Protein Data Bank with accession codes PDB: 6NB5 (LCA60) and PDB: 6NB8 (S230). The mass spectrometry data have been deposited in the ProteomeXchange consortium (PRIDE) databank with accession codes PRIDE: PDX010494. A list of software used in this study can be found in the Key Resources Table.

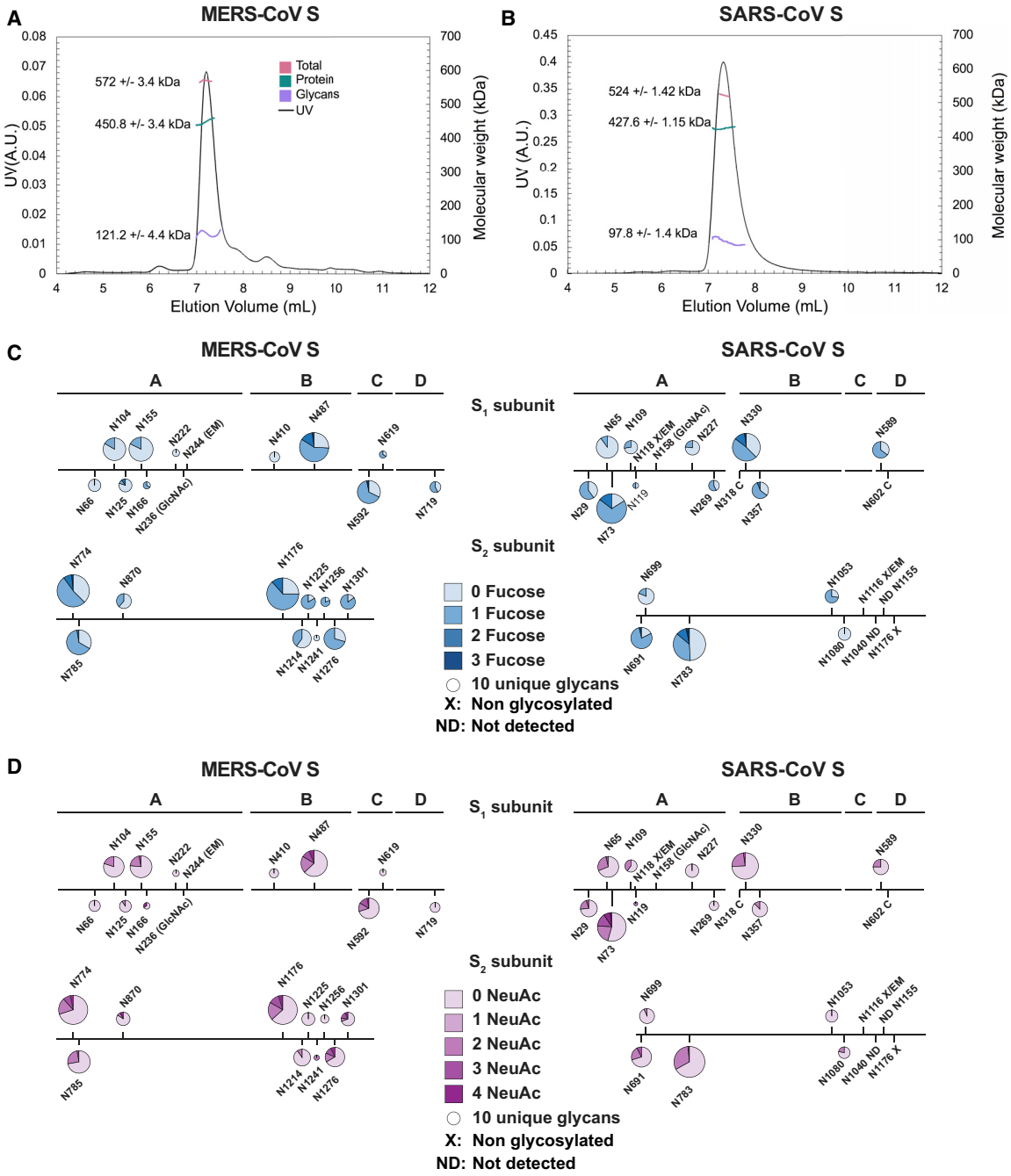

Figure S1. Characterization of the Fine Molecular Structure of the MERS-CoV and SARS-CoV S Glycan Shields, Related to Figure 1

(A-B) Quantification of the molecular weight fraction contributed by the N-linked carbohydrates decorating the MERS-CoV (A) and SARS-CoV (B) S glycoproteins expressed using HEK293F cells. Molecular weight estimates were determined using size-exclusion chromatography coupled with multi-angle light scattering, refractometry and UV spectrophotometry(Veesler et al., 2009). (C-D) LC-MS/MS analysis of the fucosylation (C) and sialylation (D) content of the MERS-CoV S 2P and SARS-CoV S 2P ectodomain glycans (in-solution digests). Each N-linked glycosylation site is represented by a pie chart colored according to the number of fucose or sialic acid moieties detected and for which the diameter is scaled based on the number of unique glycopeptides identified. NeuAc: N-acetyl-neuraminic acid.

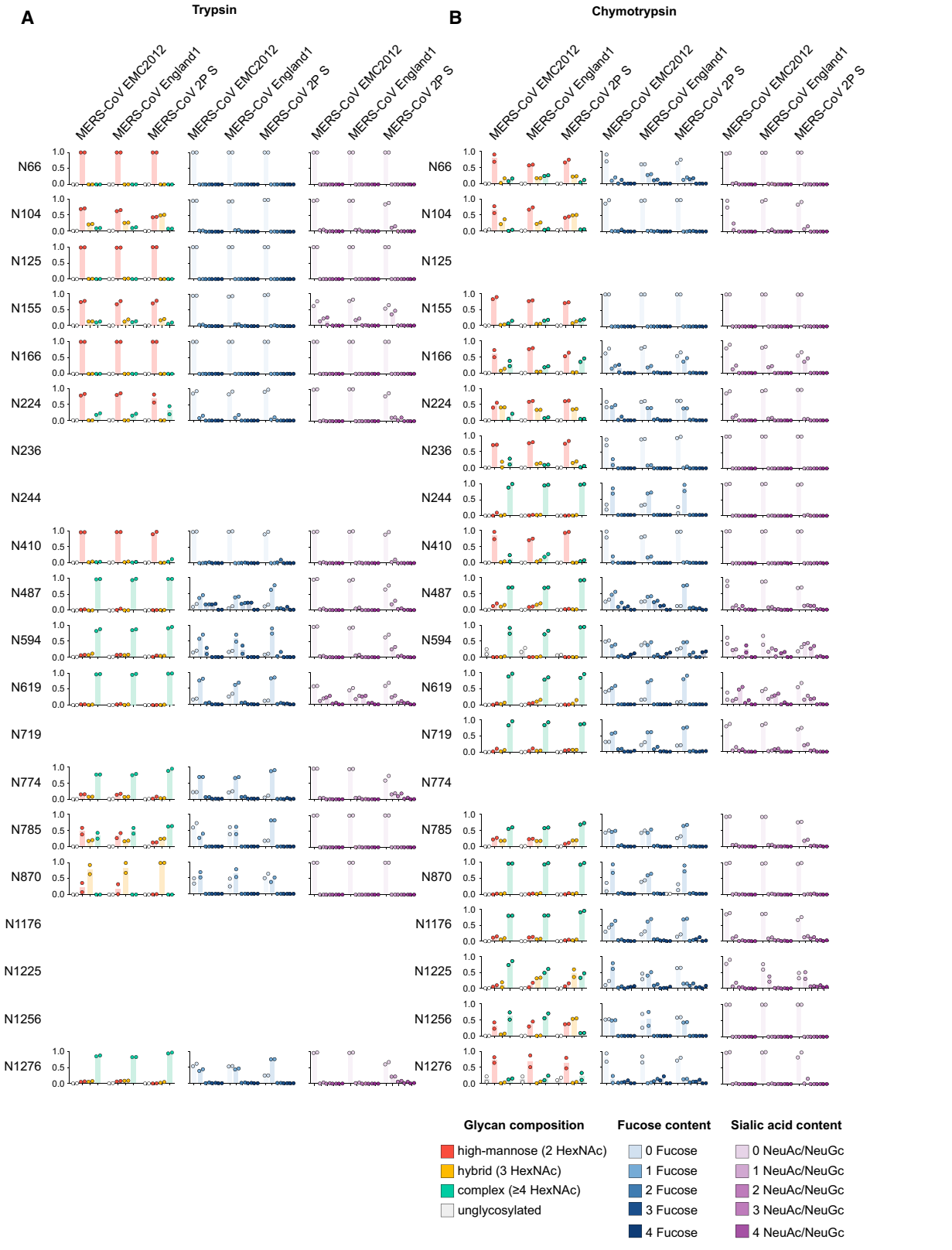

(legend on next page)

Figure S2. Comparison of Glycans N-Linked to Full-Length MERS-CoV S Incorporated in Authentic Virions and to a Purified Ectodomain. Related to Figure 1

(A-B) LC-MS/MS analysis of S oligosaccharides from MERS-CoV England1 and EMC/2012 virions as well as MERS-CoV S 2P ectodomain trimer (in-gel digests). Colored dots represent individual technical replicate values and histograms represent the experimental mean signal of the relative integrated MS1 peak areas for each glycopeptide upon trypsin (A) or chymotrypsin digestion (B). NeuAc: N-acetyl-neuraminic acid, NeuGc: N-glycolyl-neuraminic acid.

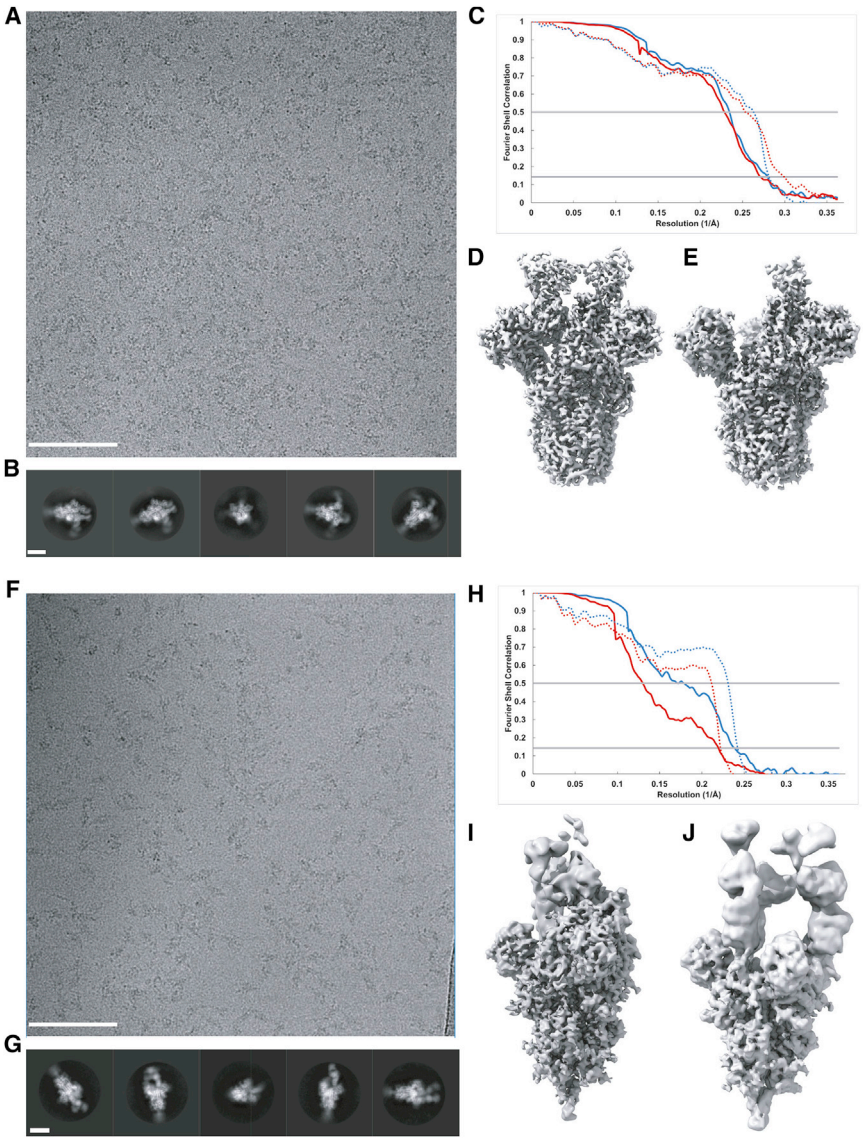

Figure S3. CryoEM Characterization of the MERS-CoV S Glycoprotein in Complex with the LCA60 Fab Fragment (A-E) and the SARS-CoV S Glycoprotein in Complex with the S230 Fab Fragment (F-J), Related to Figures 2, 3, and 4

(A) Representative micrograph. Scale bar is 100 nm. (B) Reference-free 2D class averages. Scale bar is 100 Å. (C) Gold standard (solid lines) and map/model (dotted lines) Fourier shell correlation curves for the state 1 (blue lines) or state 2 (red lines) reconstructions. (D-E) Reconstructions for state 1 (D) and state 2 (E). (F) Representative micrograph. Scale bar is 100 nm. (G) Reference-free 2D class averages. Scale bar is 100 Å. (H) Gold standard (solid lines) and map/model (dotted lines) Fourier shell correlation curves for the state 1 (blue lines) or state 2 (red lines) reconstructions. (I-J) Reconstructions for state 1 (I) and state 2 (J).

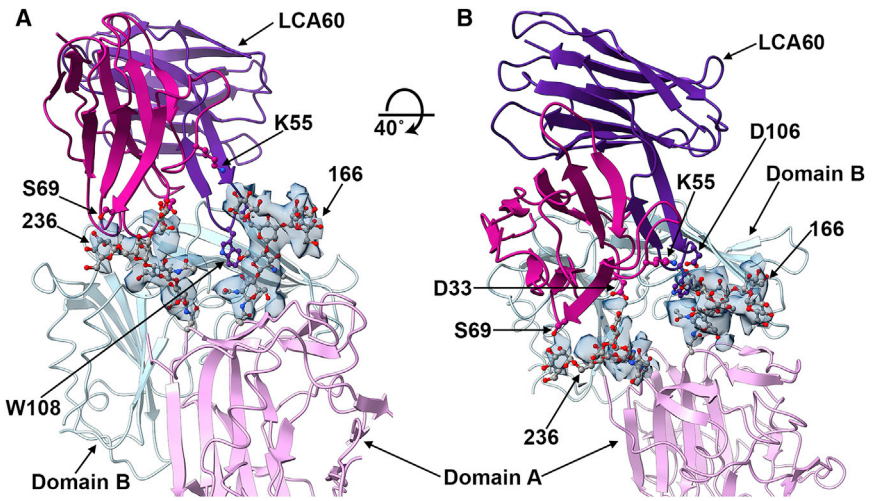

Figure S4. LCA60 Interactions with MERS-CoV S Involve N-Linked Glycans, Related to Figures 2 and 3

(A-B) Ribbon diagrams of LCA60 binding to a closed B domain. The A domain from a neighboring protomer is also shown. LCA60 residues interacting or putatively interacting with the glycans at positions N236 and N166 are shown in ball and stick representation (blue: nitrogen, red: oxygen, gray: carbon). LCA60 atoms are colored identically except for carbon atoms that are pink/purple. The color scheme is identical to Figure 2. Selected glycans are labeled based on the N-linked glycosylation sequon numbering. Only the LCA60 variable domains are shown. The cryoEM density corresponding to glycans at positions N166 and N236 is shown as a transparent blue surface.

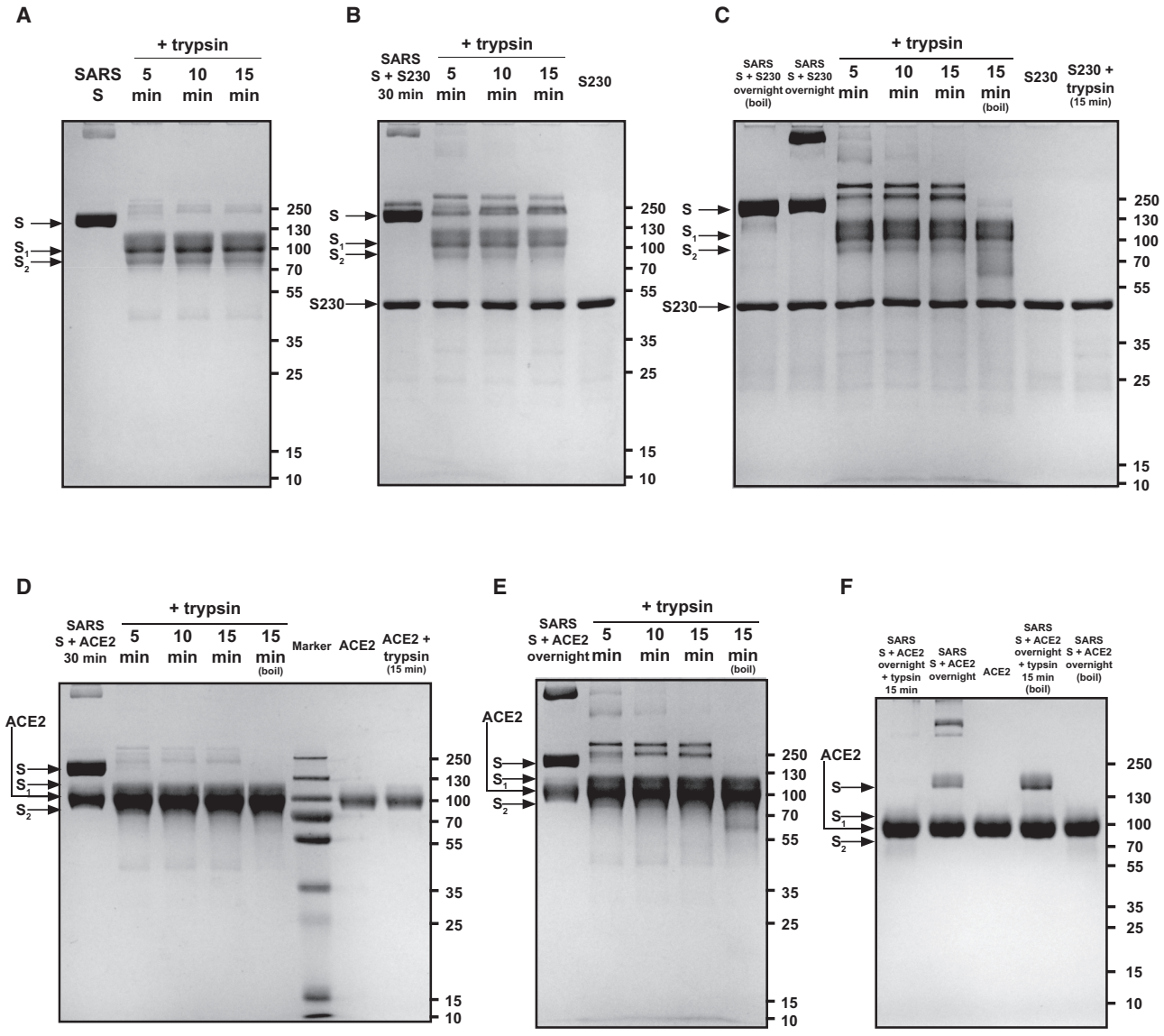

Figure S5. SDS-PAGE Analysis of SARS-CoV S Cleavage by Trypsin, under Limited-Proteolysis Conditions, in the Presence and Absence of S230 or ACE2, Related to Figure 6

(A-C) Wild-type SARS-CoV S ectodomain trimer at 7.5 μM (protomer concentration) was cleaved with 1.6 μg/mL of trypsin either directly (A), or after incubation with an equimolar concentration of Fab S230 for 30 min (B) or 30 hr (C). (D-F) Wild-type SARS-CoV S ectodomain trimer at 7.5 μM (protomer concentration) was cleaved with 1.6 μg/mL of trypsin after incubation with an equimolar concentration of the ACE2 ectodomain for 30 min (D) or 30 hr (E) or after incubation with 30 μM of the ACE2 ectodomain for 30 hr (F). Boil indicates that the sample was boiled for one minute in SDS-PAGE loading buffer prior to migration.

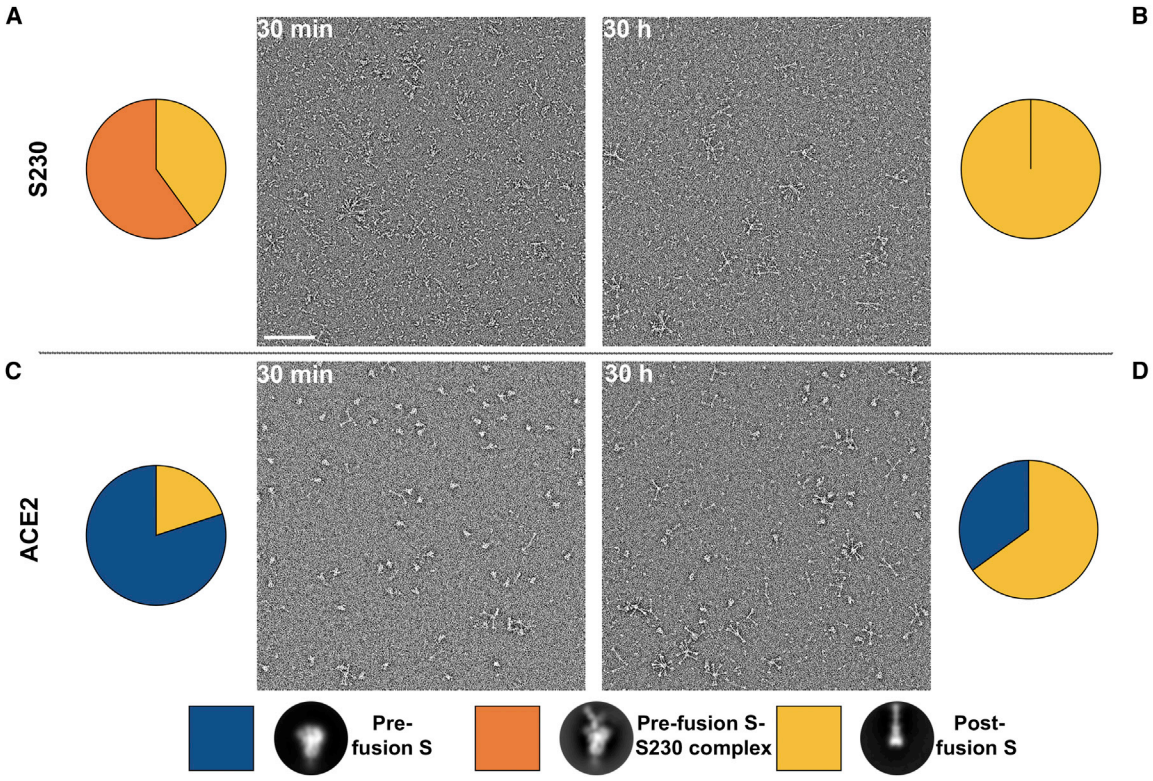

Figure S6. Effect of S230 or ACE2 on Fusogenic Conformational Changes of Pre-cleaved SARS-CoV S, Related to Figure 6

The effect of Fab S230 (A-B) or of the ACE2 ectodomain (C-D) on the conformational state of the wild-type SARS-CoV S ectodomain trimer was analyzed using single-particle electron microscopy of negatively stained samples. (A-D) Estimates of the fraction of particles corresponding to each state are represented as pie charts based on the number of particle images clustered in each group after reference-free 2D classification. Only prefusion and postfusion conformations were included in the calculations and the results are rendered using bins with a minimal width of 5%.

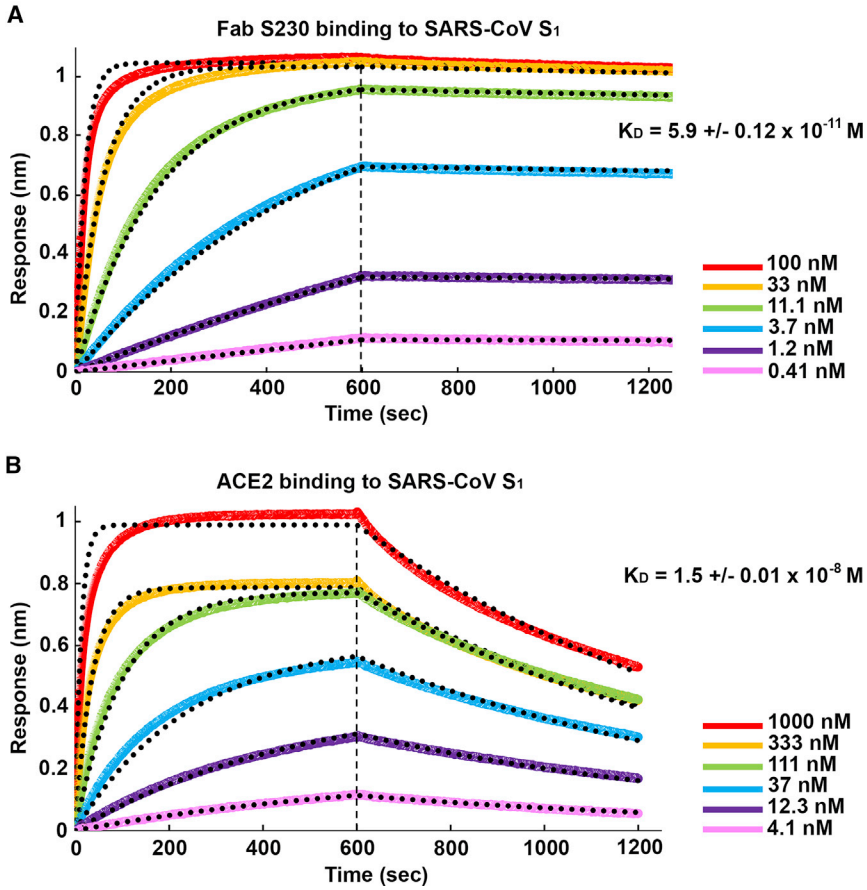

Figure S7. Biolayer Interferometry Analysis of S230 and ACE2 Binding to the SARS-CoV S_1 Subunit, Related to Figure 6

The SARS-CoV S_1 subunit was immobilized using amine coupling on ARG2 biosensors and binding of the S230 Fab (A) or the ACE2 ectodomain (B) at multiple concentrations were monitored. Equilibrium constants of dissociation and estimated errors using a global fit are indicated. The concentrations of S230 Fab or ACE2 ectodomain injected are indicated on each panel. Global fit curves are shown as black dotted lines. The vertical dashed lines indicate the transition between association and dissociation phases.

Update

Cell

Volume 183, Issue 6, 10 December 2020, Page 1732

DOI: https://doi.org/10.1016/j.cell.2020.11.031

CellPress

Cell

Correction

Unexpected Receptor Functional Mimicry Elucidates Activation of Coronavirus Fusion

Alexandra C. Walls, Xiaoli Xiong, Young-Jun Park, M. Alejandra Tortorici, Joost Snijder, Joel Quispe, Elisabetta Cameroni, Robin Gopal, Mian Dai, Antonio Lanzavecchia, Maria Zambon, Félix A. Rey, Davide Corti, and David Veesler*

*Correspondence: dveesler@uw.edu

https://doi.org/10.1016/j.cell.2020.11.031

(Cell *176*, 1026–1039.e1–e15; February 21, 2019)

We recently discovered that the purified ACE2 ectodomain used in the manuscript encompasses residues 19–741 of macaque ACE2 instead of residues 1–615 of human ACE2. Although the binding interface is conserved, the presence of the endogenous ACE2 dimerization domain affects the affinities reported in Figure S7 due to avidity. New measurements were carried out with the human ACE2 ectodomain (residues 19–615), and the corresponding binding affinities for the RBD were corrected (Starr, T.N., et al. (2020). Deep Mutational Scanning of SARS-CoV-2 Receptor Binding Domain Reveals Constraints on Folding and ACE2 Binding. Cell 182, 1295–1310. 10.1016/j.cell.2020.08.012). Our conclusions remain unchanged. We apologize for any confusion that this error may have caused.

